6-9-2016

Investigation of Infrared Detectors Based on the Gallium-free Superlattice

Theodore Schuler-Sandy

Theodore Lyman Schuler-Sandy

Candidate

Electrical and Computer Engineering

Department

This dissertation is approved, and it is acceptable in quality and form for publication:

Approved by the Dissertation Committee:

Dr. Sanjay Krishna, Chair

Dr. Elizabeth Steenbergen, Member

Dr. Ganesh Balakrishnan, Member

Dr. Mansoor Sheik-Bahae, Member

Investigation of Infrared Detectors Based on the Gallium-free Superlattice

by

Theodore Schuler-Sandy

B.S. Electrical Engineering,
New Mexico Institute of Mining and Technology, 2008

M.S. Electrical Engineering,
New Mexico Institute of Mining and Technology, 2010

DISSERTATION

Submitted in Partial Fulfillment of the

Requirements for the Degree of

Doctor of Philosophy
Engineering

The University of New Mexico

Albuquerque, New Mexico

May, 2016

Dedication

Dedicated to my mother, Alison Schuler, and my father, Lyman Sandy.

Acknowledgments

I am grateful for all the help and support given to me by many people. My advisor, Dr. Sanjay Krishna, has given me an incredible amount of encouragement and guidance, and I would not be at this point without his help. I would also like to acknowledge my committee, Dr. Ganesh Balakrishnan, Dr. Elizabeth Steenbergen, and Dr. Mansoor Sheik-Bahae, for guiding me in my efforts, and for their advice on my work.

I would like to give particular thanks to Dr. Tom Rotter, Dr. Elena Plis, and Dr. Ganesh Balakrishnan for teaching me the art of MBE growth and reactor maintenance, and for all their help throughout the course of my graduate career. I am grateful for the support of the people at CHTM, and in particular the current and former members of my research group, the MBE lab, and my office (room 117). I would like to give special thanks to Happy, Myers, SPRC, Pankaj, Brianna, Ali, Lilian, Orlando, Sen, Andrew, John, Clark, Marziyeh, Nutan, Ajit, Ha Sul, Jun Oh, David, Maya, Emma, Victor, Noel, Tom, Dan, Joel, Jannell, Chris, and Mitch. Thank you all for helping me through the PhD program, and for making my time at CHTM memorable!

I cannot forget all that my family has done to support me throughout my life. I would never have made it this far without the constant support and encouragement of my mom, Alison Schuler. I will always cherish the memories of my grandparents and my father, and hope that they would be proud of my accomplishments. I will also be forever grateful for the support given to me by Rhonda and Robert, who have been there for me since I was born.

Last but not least I would like to thank all my friends, both old and new, who have supported me. Thank you especially to Travis, Jeff, Jamey, Alex, Ben M, Ben P, and the folks at Stone Age.

Investigation of Infrared Detectors Based on the Gallium-free Superlattice

by

Theodore Schuler-Sandy

B.S. Electrical Engineering,

New Mexico Institute of Mining and Technology, 2008

M.S. Electrical Engineering,

New Mexico Institute of Mining and Technology, 2010

Ph. D., Engineering, University of New Mexico, 2016

Abstract

Infrared detection has proven to be an essential capability in a variety of fields, primarily the medical and defense fields. The current industry standard material is HgCdTe, which has been developing since its inception in the late 1950s. SLS materials are created from very thin layers, on the order of several to several tens of atomic monolayers, of two different bulk materials. These layers are alternated periodically, which results in entirely new material properties. The most common variety of SLS is the InAs-GaSb SL. This material shows great promise, but has not yet exceeded the performance of MCT detectors. This is due to the fact that the performance of the InAs-GaSb SL is limited by its Shockley-Reed-Hall (SRH) carrier lifetime. A new type of SLS, called the Ga-free SL, has demonstrated a much longer SRH lifetime, and has the potential to exceed the performance of the InAs-GaSb

SL. The focus of this dissertation is the use and optimization of the Ga-free SLS in infrared detectors. This optimization is accomplished though a series of studies that focus on several aspects of growing Ga-free SL-based detectors, including

1. Initial device characterization
2. Doping level in the detector absorber region
3. As:In BEP ratio
4. MMBE-based InAs-InSb vs. ternary InAsSb growth
5. InAs-on-InAsSb interface optimization

The first electrical characterizations of a Ga-free SL detector are reported from the initial device. This device was a MWIR PIN design created from a 14ML InAs - 12ML $InAs_{0.65}Sb_{0.35}$ superlattice. The results of this showed an unexpectedly high level of dark current. The cause of this current was investigated using a curve-fitting program provided by IRNova, which showed that trap-assisted tunneling may be the cause of this result.

The next study compared varied levels of doping in the absorber region of a Ga-free SL MWIR PIN detector. The designs for these devices were similar to the initial device, but the InAsSb composition was changed to be $InAs_{0.81}Sb_{0.19}$, which provided a better lattice match to the GaSb substrate. The absorber regions were doped at NID (reference), $5{\cdot}10^{15}$, $1{\cdot}10^{16}$, and $3{\cdot}10^{16}$ cm^{-3} p-type. P-type doping was chosen to offset the intrinsic n-type behavior of the Ga-free material. The results showed that the highest doping level, at $3{\cdot}10^{16}$ cm^{-3}, resulted in the lowest dark current (0.00248 vs. 0.08353 A/cm^2 for the best device from each sample). The quantum efficiency for this device was slightly reduced from the reference sample, (37.4% vs. 42.4%), as a tradeoff for the reduced dark current levels. The dark current levels of these devices were reduced as the doping increased, thereby indicating G-R dominance.

The BEP ratio study tested several As:In ratios with the purpose of optimizing the growth conditions for an MWIR Ga-free SL. This study performed electrical characterization on three samples with BEP ratios of 5:1, 6:1, and 7:1. These devices were grown using the same MWIR PIN design used in the doping study. Both quantum efficiency and dark current levels from these devices indicated that the 7:1 As:In BEP ratio was an improvement on the lower ratios.

The fourth study discussed in this dissertation compared an MWIR Ga-free SL grown using an MMBE-grown InAs-InSb alloy in place of the InAsSb ternary material with an MWIR Ga-free reference sample. The purpose of this was to determine if the use of the MMBE technique during growth had adverse effects on the electrical performance of the resulting detectors. However, the dark current of the MMBE-based device was lower than the reference sample (0.0853 vs. 0.1227 A/cm^2 at -10mV bias and 80K), and the quantum efficiency was higher (39.7% vs. 24.1% at -10mV bias and 80K). This indicated that MMBE may improve the resulting devices, rather than detract from their performance.

The final study tested a series of interface layers placed at the InAs-on-InAsSb interface. This was intended to minimize the diffusion of Sb from the InAsSb layer into the following InAs layer. These samples were the same design as used in previous studies, with the exception that the InAsSb layers were all replaced with MMBE InAs-InSb (as tested in the MMBE study). The interface layers tested were a 1 second growth interrupt, a 1 second As soak, a 1 second Al flash, and a 1ML AlSb layer. A reference sample with no special interface layer was also grown. The results showed that the reference, the As soak, and the AlSb layer all showed comparable performance, whereas the Al flash and growth interrupt reduced the quality of the resulting devices. From the resulting data, further study of the use of an As soak is encouraged.

Contents

List of Figures

List of Tables

List of Tables

Chapter 1

Introduction

Infrared detectors have found numerous uses in modern technology, primarily in the medical and defense fields. The applications for these detectors include chemical detection, night vision, medical diagnosis, and thermophotovoltaic power production. The operation of infrared detectors is similar to that of a digital camera, though the materials used to make the sensor are different. Conventional cameras use silicon to make the detectors, since silicon is sensitive to the visible light band. Infrared is a much broader spectrum than visible light, so the material used to make an infrared detector will depend on the desired wavelength or wavelength range. Infrared is typically split up into several sub-bands, including: Near Infrared (NIR), Shortwave Infrared (SWIR), Midwave Infrared (MWIR), Longwave Infrared (LWIR), the Very Longwave Infrared (VLWIR), and the Far Infrared (FIR). The wavelength ranges associated with these sub-bands are: 700nm to 1.5μm (NIR), 1.5μm to 3μm (SWIR), 3μm to 8μm (MWIR), 8μm to 12μm (LWIR), 12μm to 32μm (VLWIR), 32μm to 1mm (FIR).

A number of different materials exist for detecting infrared light. Materials like InGaAs and InSb are commonly used for SWIR to MWIR detection. HgCdTe,

sometimes called MCT, is the current standard for MWIR and LWIR detection. However, MCT exhibits a high degree of Auger recombination (which is described in more depth elsewhere [1]). This induces a higher level of dark current in the resulting infrared detectors than is desired. A newer material, called the strained-layer superlattice (SLS), has demonstrated the ability to suppress Auger recombination, which gives it the potential to outperform MCT detectors[2, 3, 4].

Strained-layer superlattices are created from very thin layers of two distinct materials. Most commonly, these materials are InAs and GaSb. By alternating these two materials to create a periodic structure, a new material can be created. Superlattices are very effective as an infrared detector material, since the wavelength to which they are sensitive can be altered by varying the thickness of the two constituent layers. However, superlattices exhibit a different process called Shockley-Reed-Hall (SRH) recombination, which has prevented them from exceeding the performance of current MCT detectors, as described by Rule 07[5]. Improving this carrier lifetime, and thereby reducing the dark current arising from the Generation-Recombination (GR) process, is a major focus of current IR detector research. In more recent times, a new superlattice material, the gallium-free superlattice (or Ga-free SL), has emerged. This superlattice is composed of InAs and InAsSb, and has been shown to have a much longer SRH lifetime (and thus the potential for a much lower dark current) than the InAs-GaSb superlattice [6, 7, 8, 9].

This dissertation describes a series of experiments aimed at improving the growth of Ga-free superlattice material-based infrared detectors. The two primary goals are the reduction of dark current and the improvement of quantum efficiency demonstrated by these devices. The results presented here demonstrate several methods of accomplishing these goals.

Chapter 2 provides background information on a variety of subject matters that are relevant to understanding the Ga-free SL. The subjects include the Ga-free SL,

crystal growth primarily focusing on molecular beam epitaxy (MBE), and the characterization of grown devices.

An initial Ga-free SL-based detector is described in chapter 3. This detector was designed to be an MWIR PIN structured device in order to test the electrical characteristics of the Ga-free SL material. The dark current and quantum efficiency results from this device are reported in this chapter.

Chapter 4 covers a study in which the absorber layers in a series of MWIR PIN Ga-free SL-based detectors are doped with a light p-type doping. Several levels of doping are compared using dark current and quantum efficiency as metrics for device performance.

Chapter 5 discusses a series of devices grown to optimize the As:In BEP ratio used during growth of the Ga-free SL. The electrical characterizations of these devices are presented and compared.

Chapter 6 presents the use of modulated MBE (MMBE) grown InAs-InSb material in place of the InAsSb ternary material normally present in the Ga-free SL. This chapter discusses the MMBE process, and provides the design used in an MWIR PIN device. The electrical characterizations of this device are provided, and compared to those of a reference sample.

Chapter 7 is focused on a study seeking to improve the InAs-on-InAsSb interface present in the Ga-free SL. Several different layers are added to attempt to reduce the diffusion of Sb from an InAsSb layer into the following InAs layer. As with previous studies, MWIR devices are grown in order to compare the performance of each interface layer.

The final chapter provides conclusions and discusses future work.

Contributions of this work:

- Initial electrical characterizations of a device based on the Ga-free SL
- Initial investigation of the effect of a light p-type doping in the absorber region of a MWIR Ga-free SL detector
- Optimization of the As:In BEP ratio used during Ga-free SL growth
- A comparison of a device grown using MMBE-based InAs-InSb material to one grown using the InAsSb ternary material
- An investigation of methods for improving the InAs-on-InAsSb interface in the Ga-free SL

Publications:

- T. Schuler-Sandy, M. Malone, Z.-B. Tian, L. Treider, E. Plis, T. Rotter, C. Morath, V. Cowan, and S. Krishna, "Gallium free type II InAs/$InAs_xSb_{1-x}$ superlattice photodetectors," *Applied Physics Letters*, vol. 101, 2012
- T. Schuler-Sandy, B. Klein, L. Casias, S. Mathews, C. Kadlec, Z.-B. Tian, E. Plis, S. Myers, and S. Krishna, "Growth of InAs-InAsSb SLS through the use of digital alloys," *Journal of Crystal Growth*, vol. 425, pp. 29-32, 2015
- E. A. Plis, T. Schuler-Sandy, D. A. Ramirez, S. Myers, and S. Krishna, "Dark current reduction in InAs/InAsSb superlattice mid-wave infrared detectors through restoration etch," *Electronics Letters*, Oct. 2015
- Z.-B. Tian, T. Schuler-Sandy, S. Krishna, D. Tang, and D. J. Smith, "Molecular beam epitaxy growth of antimony-based mid-infrared interband cascade photodetectors," *Journal of Crystal Growth*, vol. 425, pp. 364-368, 2015
- Z.-B. Tian, T. Schuler-Sandy, and S. Krishna, "Dark current in antimony-based mid-infrared interband cascade infrared photodetectors," *Infrared Physics & Technology*, vol. 70, pp. 44-47, 2015

- Z.-B. Tian, T. Schuler-Sandy, S. E. Godoy, H. S. Kim, and S. Krishna, "High-operating-temperature MWIR detectors using type II superlattices," *Proceedings of the SPIE*, vol. 8867, 2013

- Z.-B. Tian, T. Schuler-Sandy, and S. Krishna, "Electron barrier study of mid-wave infrared interband cascade photodetectors," *Applied Physics Letters*, vol. 103, 2013

- Z.-B. Tian, T. Schuler-Sandy, S. E. Godoy, H. S. Kim, J. Montoya, S. Myers, B. Klein, E. Plis, and S. Krishna, "Quantum-engineered mid-infrared type-II InAs/GaSb superlattice photodetectors for high temperature operations," *Proceedings of the SPIE*, vol. 8704, 2013

- Z.-B. Tian, T. Schuler-Sandy, S. E. Godoy, H. S. Kim, J. Montoya, and S. Krishna, "Mid-wave infrared interband cascade photodetectors and focal plane arrays based on InAs/GaSb superlattices," *Photonics Conference (IPC), 2013 IEEE*

- A. Kazemi, M. Zamiri, J. O. Kim, T. Schuler-Sandy, and S. Krishna, "Colloidal and Epitaxial Quantum Dot Infrared Photodetectors: Growth, Performance, and Comparison," *Wiley Encyclopedia of Electrical and Electronics Engineering*, pp. 1-26, 2014

- Z.-B. Tian, S. E. Godoy, H. S. Kim, T. Schuler-Sandy, J. A. Montoya, and S. Krishna, "High operating temperature interband cascade focal plane arrays," *Applied Physics Letters*, vol. 105, 2014

- B. Klein, N. Gautam, E. Plis, T. Schuler-Sandy, T. J. Rotter, S. Krishna, B. C. Connelly, G. D. Metcalfe, P. Shen, and M. Wraback, "Carrier lifetime studies in midwave infrared type-II InAs/GaSb strained layer superlattice," *Journal of Vacuum Science and Technology B*, vol. 32, 2014

- E. A. Plis, N. Gautam, M. N. Kutty, S. Myers, B. Klein, T. Schuler-Sandy, M. Naydenkov, and S. Krishna, "Performance of long-wave infrared InAs/GaSb strained layer superlattice detectors for the space applications," *Proceedings of the SPIE* vol. 8164, 2011

- A. G. Unil Perera, Y.-F. Lao, S. Wolde, Y. H. Zhang, T. M. Wang, J. O. Kim, T. Schuler-Sandy, Z.-B. Tian, and S. Krishna, "InAs/GaAs quantum dot and dots-in-well infrared photodetectors based on p-type valence-band intersublevel transitions," *Infrared Physics & Technology*, vol. 70, pp. 15-19, 2015

- S. Wolde, Y.-F. Lao, A. G. Unil Perera, Y. H. Zhang, T. M. Wang, J. O. Kim, T. Schuler-Sandy, Z.-B. Tian, and S. Krishna, "High temperature terahertz response in a p-type quantum dot-in-well photodetector," *Applied Physics Letters*, vol. 105, 2014

- Y.-F. Lao, S. Wolde, A. G. Unil Perera, Y. H. Zhang, T. M. Wang, J. O. Kim, T. Schuler-Sandy, Z.-B. Tian, and S. Krishna, "Study of valence-band intersublevel transitions in InAs/GaAs quantum dots-in-well infrared photodetectors," *Applied Physics Letters*, vol. 104, 2014

- L. Acosta, B. Klein, Z.-B. Tian, E. Frantz, S. Myers, N. Gautam, T. Schuler-Sandy, E. Plis, and S. Krishna, "Investigation of quantum efficiency in mid-wave infrared (MWIR) InAs/GaSb type-II strained layer superlattice (T2SL) detectors," *Proceedings of the SPIE*, vol. 8996, 2014

- Y.-F. Lao, S. Wolde, A. G. Unil Perera, Y. H. Zhang, T. M. Wang, H. C. Liu, J. O. Kim, T. Schuler-Sandy, Z.-B. Tian, and S. Krishna, "InAs/GaAs p-type quantum dot infrared photodetector with higher efficiency," *Applied Physics Letters*, vol. 103, 2013

- S. Myers, E. Plis, C. Morath, V. Cowan, N. Gautam, B. Klein, M. N. Kutty, T. Schuler-Sandy, M. Naydenkov, and S. Krishna, "Comparison of superlattice

based dual color nBn and pBp infrared detectors," *Proceedings of the SPIE*, vol. 8155, 2011

Conference Presentations:

- T. Schuler-Sandy, S. Myers, B. Klein, N. Gautam, P. Ahirwar, Z-B. Tian, T. Rotter, G. Balakrishnan, E. Plis, and S. Krishna, "Absorber Doping in Gallium-Free Superlattice Photodetectors." Presented at the US Workshop on the Physics & Chemistry of II-VI Materials, Chicago, Il., Oct. 2013
- N. Gautam, A. V. Barve, S. Myers, B. Klein, E. Plis, M. Naydenkov, M. N. Kutty, T. Schuler-Sandy, and S. Krishna, "Polarization selective interband transitions in type-II InAs/GaSb superlattices," *IEEE Photonic Society 24th Annual Meeting*, 2011
- E. Plis, N. Gautam, B. Klein, S. Myers, T. Schuler-Sandy, M. N. Kutty, Z.-B. Tian, and S. Krishna, "Performance of single-and dual-color detectors using InAs/GaSb strained layer superlattices," Presented at the Lester Eastman Conference on High Performance Devices (LEC), Singapore, 2012

Chapter 2

Background

2.1 Infrared (IR)

All objects above 0K emit light, the wavelength of which is dependent on the temperature of the object. This is called blackbody radiation. An object at or around room temperature will emit light in the infrared (IR) regime. IR light refers to a spectrum of light that extends out past visible red light, encompassing wavelengths from roughly 800nm up to 1mm. This spectrum is further split into subcategories that include the near infrared (NIR) that extends from 700nm to 1.5μm, the shortwave infrared (SWIR) from 1.5μm to 3μm, the midwave infrared (MWIR) from 3μm to 8μm, the longwave infrared (LWIR) from 8μm to 12μm, the very long wavelength infrared from 12μm to 32μm, and the far infrared (FIR) which covers 32μm to 1mm. These splits are determined by transmission windows in the atmosphere [10, 11, 12]. The regime in which an object emits depends on its temperature. For instance, a hot car engine will emit in the SWIR to NIR range, whereas a human body will emit in the LWIR range. This is governed by the following laws:

1. **Planck's law**

The distribution of wavelengths emitted by a blackbody object, also called the spectral radiance, at a certain temperature is defined by Planck's law, which is as follows:

$$W(\lambda, T) = \frac{2hc^2}{\lambda^5} \cdot \frac{1}{e^{\frac{hc}{\lambda k_B T}} - 1} \tag{2.1}$$

In this equation, h is Planck's constant, k_B is Boltzmann's constant, T is temperature, c is the speed of light in a vacuum, λ is wavelength in μm, and W is given in $\mathrm{W/m^2/\mu m}$.

2. **Stefan-Boltzmann law**

   The Stefan-Boltzmann law describes the thermal energy per time per area radiated by an object. This is given as follows:

   $$P/A = e\sigma T^4 \tag{2.2}$$

   where P is the power, A is the area, e is the emissivity of the object ($e = 1$ for blackbodies), σ is the Stefan-Boltzmann constant, and T is the temperature of the object.

3. **Wien's displacement law**

   Wien's law states that the peak emission wavelength for a blackbody is inversely proportional to its temperature. This is enumerated as follows:

   $$\lambda_P = b/T \tag{2.3}$$

   where λ_P is the peak emission wavelength, T is the temperature, and b is a constant called Wien's displacement constant, which is equal to $2898 \cdot \mu\mathrm{m} \cdot \mathrm{K}$.

2.2 IR Photodetectors

The ability to detect light in the infrared has numerous applications in the medical, meteorological, power generation, and defense fields. However, this ability is not in-

nate to humans, and thus technology has been developed to provide this capability. There are multiple methods of IR detection, including both thermal detectors and photodetectors. The primary focus of this thesis is in the area of photovoltaic photodetectors. Discussions of the other varieties of detectors can be found in previous theses [10, 11].

A photodetector is a type of device that is able to convert incident photons into another useful form. Typically this form is an electrical current, which can then be read by associated circuitry. A common type of photodetector is the silicon-based detector used in digital cameras to capture visible light. Solar cells are another example. In both these cases, the aim is to absorb photons with wavelengths in the visible range and convert them into an electrical current. This can be accomplished by taking advantage of the photovoltaic effect, in which photons incident on the detector interact with electrons present in the detector to create an electrical current. The particular wavelengths at which this can occur for a given semiconductor material is defined by its bandgap. This bandgap is determined by the energy level difference between the lowest energy level in the conduction band and the highest level in the valance band. This is an intrinsic property of the material. When a photon interacts with an electron in the material, the energy from the photon is absorbed and transferred to the electron. If the photon has enough energy to cause the electron to excite into an available energy level in the conduction band, it can be used to create a current through the device. However, this will not occur in a bulk material alone. In semiconductor devices, the current is achieved through the principle of material doping. In order to dope a material, a trace amount of another material is embedded randomly throughout a given layer of the device. This trace material will have either one more electron (n-type) or one fewer electron (p-type) than the detector material. The most basic type of photodiode is a PN junction device, which is composed of two layers. As the name implies, one layer is doped n-type and the other p-type, which creates an inherent electric field throughout the

device. When a photon of sufficient energy is absorbed in the device, an electron is excited into the conduction band and induced by this inherent electric field to move toward a contact, from which it can be extracted as a current. This, in turn, leaves behind a hole, which will move toward the opposite contact, and will also be extracted. Typically, the speed of this extraction is limited by the hole, which will move much more slowly than the electron. A bias voltage can be added to the device to further encourage (or even discourage) this process, though this is not necessary in a simple PN junction.

Semiconductor materials will typically have some form of inherent doping level associated with them. This is the result of slight imperfections in the material, which alter its electrical properties. The type of intrinsic doping level depends on the material. InAs, for instance, is n-type while GaSb is p-type. This intrinsic doping level can be countered by introducing an equivalent level of the opposite type. In some instances, this can improve the performance of a photodetector.

IR photodetectors can be tuned to certain wavelengths by varying material properties, and typically have a fast response time. However, they also require cryogenic cooling to operate [11]. A major focus is in creating high-operating temperature (HOT) IR photodetectors in order to remove the need for bulky cooling systems. Another main focus is in improving the signal-to-noise ratio (SNR) of available detectors. The SNR can generally be improved greatly by reducing the amount of noise in the detector, which can be done with novel materials and device designs. In detectors, this noise is primarily from the dark current of the detector.

Dark Current

Dark current simply refers to a current flowing through the detector when there is no light around for it to detect, thereby creating a false signal. The dark current

limits the lowest power signal that can be detected, therefore lower dark current will allow for the detection of lower power signals. There are several types of dark current inherent to infrared detectors, including diffusion dark current, generation-recombination (GR) dark current, trap assisted tunneling (TAT), and band-to-band tunneling (BTB)[13].

1. **Diffusion**

   Diffusion dark current is an intrinsic limit in a detector, and also serves as a goal for detector performance. This type of dark current is dependent on temperature and material properties, and is described as follows [14]:

   $$J_{\text{diff}} = n_i^2 \sqrt{e k_B T} \left(\frac{1}{N_A} \sqrt{\frac{\mu_e}{\tau_e}} + \frac{1}{N_D} \sqrt{\frac{\mu_h}{\tau_h}} \right) \cdot \left(e^{\frac{qV}{k_B T}} - 1 \right) \tag{2.4}$$

   In this equation, n_i is the intrinsic doping level of the material, e is the electron charge ($1.609 \cdot 10^{-19}$ coulombs), k_B is Boltzmann's constant ($1.3807 \cdot 10^{-23}$ eV/K), N_A and N_D are the number of acceptors and donors in the material, respectively, μ is the carrier mobility, τ is the carrier lifetime, T is the temperature, and V is the voltage bias.

2. **Generation-Recombination**

   GR current arises from defects in the depletion region of a device, called Shockley-Read centers. These defects provide extra energy levels in the mid-gap that make it easier for carriers to both thermally excite and recombine. This is defined as follows [15]:

   $$J_{\text{GR}} = \frac{2 n_i W k_B T}{(V_{bi} - V) \tau_{GR}} \cdot \sinh \left(\frac{qV}{2 k_B T} \right) \; for \; V < 0 \tag{2.5}$$

   In this equation, W is the depletion width, τ_{GR} is the GR lifetime in the material, and V_{bi} is the built-in voltage of the device.

3. **Trap Assisted Tunneling (TAT)**

   TAT current is created by minority carriers tunneling through a junction with

the assistance of an intermediate trap state. This trap state is typically the result of defects in the material. This is defined as follows [15]:

$$J_{\text{TAT}} = \frac{q^3 m_n^* E M^2 W N_T}{8\pi\hbar^3(E_g - E_T)} \cdot \exp\left(-\frac{4\sqrt{2m_n^*(E_g - E_T)^3}}{3q\hbar E}\right) \tag{2.6}$$

where m_n^* is the electron effective mass, W is depletion width, M is a matrix parameter, N_T is the number of traps, and E_T is the trap energy.

4. **Band-to-Band (BTB)**

   This refers to the probability that a carrier will tunnel from the valence band of a device directly to the conduction band on the other side of a junction. This is primarily dependent on the intrinsic electric field and the voltage applied to the device, and will only come into play at high bias voltages. BTB dark current is defined as follows:

$$J_{\text{BTB}} = \frac{\sqrt{2m_n^* q^3 E V}}{4\pi^3\hbar^2\sqrt{Eg}} \cdot \exp\left(-\frac{\pi^2\sqrt{m_n^* E_g^3}}{4q\hbar E}\right) \tag{2.7}$$

These equations have also been modeled directly for SL materials[16, 17]. An ideal detector will provide background-limited performance (BLIP), which occurs when the noise from the detector is due primarily to the ambient background rather than any noise in the detector itself. In the case of a real detector, this will be further limited by the quantum efficiency of the device, since a real device is not perfectly efficient.

Quantum Efficiency

The quantum efficiency of a device is effectively a measure of the probability that a photon incident on the device will cause an electron to be excited and extracted as a current. This number, without any gain in the system, will be between 0 and

1, wherein 1 refers to one electron extracted per incident photon. The quantum efficiency can be determined as follows

$$\eta = \frac{I_{ph}}{qA_d\phi} \tag{2.8}$$

In this equation, I_{ph} is the generated photocurrent, A_d is the area of the detector, and ϕ is the incident photon flux given in photons per second per square centimeter. The quantum efficiency of a device can be measured using a calibrated blackbody source that provides a known amount of power per unit area on a device.

2.2.1 IR Detector Materials

The materials used in infrared detection vary depending on the desired wavelength range. Commercially available IR detectors tend to be made from bulk II-VI or III-V materials. Prominent infrared detector materials include HgCdTe (MCT), InSb, quantum well infrared photodetectors (QWIPs), quantum dots (QDs), and strained-layer superlattices (SLSs).

The current industry standard for infrared detection is the MCT material. The dark current for this material is estimated by a metric called Rule 07 [5]. In order to improve on current MCT technology, the dark current level of the detector in question must be lower than the level defined by this curve. There are several strategies proposed to accomplish this, with the most promising technology being the strained-layer superlattice (SLS) [4, 18].

2.3 Superlattices

The primary contender for improving upon the results demonstrated by MCT materials is the strained-layer superlattice (SLS). A superlattice is a periodic structure

composed of two alternating layers. These layers are very thin, typically on the order of 5-20 atomic monolayers (MLs) each.

The initial idea for a periodic heterostructure material was first proposed in 1970 by Esaki and Tsu [19, 20]. This material requires a period thinner than the electron mean free path, which causes the system to enter a quantum regime. The idea was then formalized into the SLS material later in the 1970s by Sai-Halasz, Esaki, and Tsu [21]. The superlattice name is derived from the fact that the period of the lattice is determined by the period of the layers, rather than the lattice constant of the materials. The SLS material was later proposed for use in infrared detection by Smith and Mailhiot [2]. Since then, it has been an active topic of research.

The most common form of SLS is the InAs/Ga(In)Sb material system. In this material, thin layers of InAs and GaSb are alternated periodically to form a superlattice (SL). Since this material is grown on GaSb substrates, a thin InSb layer is often added to compensate for the strain induced by the InAs material. As noted before, the bandgap of the SL will be determined by the layer thicknesses. In a superlattice, the Brillouin zone splits into smaller minizones consisting of a series of allowed and forbidden energy bands[20]. This occurs due to the superlattice period being significantly thicker than the crystal lattice constant. The bandgap of a superlattice is determined by the separation between the upper edge of the valance band and the lower edge of the conduction band. This can be tuned over a range of 3μm to 30μm by changing the layer thicknesses, and thus the SL period, and the layer compositions [10, 22]. An example band lineup of a superlattice is shown in figure 2.1. The downside to this capability is that the optical absorption capabilities of the SL material are reduced as the layer thicknesses increase. This occurs due to the fact that absorption in an SL structure requires an overlap of electron and hole wavefunctions, which occurs primarily at the interfaces between the two materials [23]. The overall effect is that the amount of absorption per period will be lower for

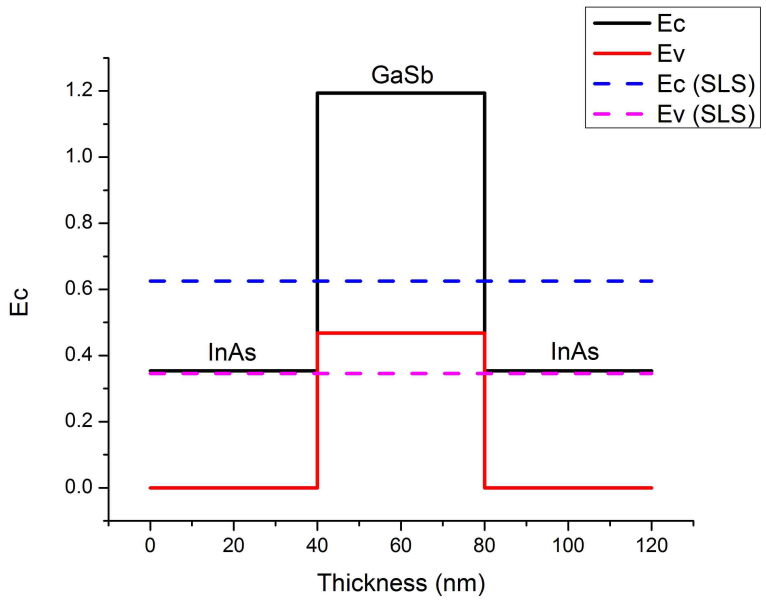

Figure 2.1: An example band lineup for an InAs-GaSb SL. The SL minibands are depicted as dotted lines, while the bulk material conduction and valence bands are solid lines. The type-II broken gap alignment can be seen between the valence band of the GaSb and the conduction band of the InAs.

SLs designed to operate at longer wavelengths.

A major benefit of the SLS material is that it suppresses interband tunneling and Auger recombination due to the strain inherent in the system [2]. The Auger recombination can be further reduced through careful band engineering [24]. Since the InAs-GaSb SL material has a larger electron effective mass ($0.04m_0$) than bulk MCT, the tunneling currents are lower than those in MCT detectors with the same bandgap [2]. Furthermore, the SLS is capable of producing better uniformity over the surface of a wafer as well as lower leakage currents [25]. This indicates that it is possible for SL materials to improve on the performance demonstrated by their MCT counterparts. However, despite recent progress made in the growth and fabrication of SL materials [9, 26, 27, 28] and band structure engineering [29, 30, 31, 32, 33,

34, 35, 36], SL materials have not yet sufficiently improved upon the performance of MCT detectors.

The dark current present in InAs-GaSb SL systems is limited by G-R dark current attributed to the presence of Shockley-Read-Hall (SRH) centers in the material [24, 37, 38]. These defects are currently associated with the GaSb layer, and have been theorized to be due to the large difference between optimal T2SL and GaSb growth conditions [1, 39]. It has been demonstrated that the SRH rate approaches a maximum when the energy level of the trap centers approach midgap [40]. Analysis of the formation energy of defects dependent on the location of the Fermi level stabilization energy has demonstrated midgap defects can form in GaAs and GaSb due to the fact that the stabilized Fermi level is located near the valence band or midgap, but not in InAs, wherein the stabilized Fermi level is located above the conduction band edge [41]. This indicates that SRH recombination through midgap trap levels can occur in GaAs and GaSb, but not in InAs. Presuming this is true, the carrier lifetime in InAs should be greater than that in GaSb. This has been experimentally demonstrated in a study that found that the carrier lifetime decreased with increasing thickness of the GaSb layer[39]. Further detail on carrier lifetimes in InAs-GaSb SL materials can be found in previous theses [1]. The large difference between the carrier lifetimes in InAs and GaSb has motivated investigation into the InAs-InAsSb, or Gallium-free, SL material.

2.4 InAs-InAsSb Superlattice

The InAs-InAsSb (or Ga-free) SL was developed initially for use in infrared lasers in the 1990s [42]. These lasers were able to demonstrate continuous-wave (CW) operation, indicating some promise in the material [43]. Initial structural characterization was performed via scanning tunneling microscopy (STM), and demonstrated mostly

sharp interfaces between the two layers, with some intermixing occurring primarily on the boundary where InAs was grown on InAsSb [44]. This incorporation is due to the intermixing of Sb into the surrounding InAs layers. The material was later proposed for use in IR detectors [45]. The Ga-free SL has shown a type-IIb band alignment, which is the same alignment shown by the InAs-GaSb SL[46, 47].

The Ga-free SL has shown considerable potential as an IR detector material. This is due to the SRH carrier lifetime in this SL being considerably longer than that in the InAs/Ga(In)Sb SL [6, 7, 8, 48, 49, 50]. The length of the SRH lifetime is expected to result in a considerably lower G-R dark current level, and thus, presuming the Ga-free SL is G-R dominated, a lower overall dark current. This belief is reinforced by studies demonstrating that the Ga-free SL material shows good Auger suppression [51, 52, 53]. Since many of the lifetime studies depend on photoluminescence measurement, the effect of AlSb barriers on the carrier lifetime in Ga-free SLs has been studied[54]. Due to this, some groups have begun to develop Ga-free SL detector devices. Also, the bandgap range over which the superlattice can be tuned has been shown to be reasonably wide [47, 55]. Most research has focused on the creation of nBn devices, which have shown a very low dark current, but also a low quantum efficiency (QE) [56]. PIN structure devices show relatively high dark current, which isn't entirely unexpected due to the lack of a barrier, but have also shown a higher quantum efficiency in MWIR [57, 58] and VLWIR [8]. More recent research has shown that a restoration etch may improve the dark current level in these devices [59]. One two-color (MWIR/LWIR) nBn-based device has been demonstrated as well [60].

2.5 Semiconductor Crystal Growth

The growth of semiconductor devices can be achieved in several different ways. The two most common methods for growing quantum structures are metal organic chem-

ical vapor deposition (MOCVD), also sometimes referred to as metalorganic vapor phase epitaxy (MOVPE), and molecular beam epitaxy (MBE). Each technique has merits and flaws, and whether one or the other is preferred highly depends on the desired material and device structure.

2.5.1 MOCVD

MOCVD is commonly used in commercial applications due to the relatively low cost of production and the relatively high growth rate for materials. This technique relies on inducing chemical reactions and thereby depositing material on the surface of a substrate. Since this process requires thermodynamic equilibrium, MOCVD is able to produce very high quality materials. This can further be done at a higher rate than is achievable via MBE. However, the trade-off is that the interfaces will not be as controlled as they can be in an MBE.

In MOCVD, the material to be grown is delivered to the substrate by using precursor gases containing the desired elements. These elements are delivered to the substrate, where they react with each other above a heated substrate. Group III elements commonly use methyl groups as precursors, and group V elements commonly use hydrogen. When these chemicals reach the heated substrate, the molecules decompose through a process called pyrolysis. Once split from the precursor, the desired element is deposited on the surface of the wafer. It is important in MOCVD to maintain equilibrium in order to produce high quality crystal structures. There have been several growths of Ga-free SL using MOCVD [61, 62], though the primary focus of this dissertation is molecular beam epitaxy (MBE).

2.5.2 Molecular Beam Epitaxy

MBE is a technique used commonly to grow quantum structures that require very fine interface control. In this technique, materials are heated under ultra-high vacuum (UHV) conditions to form material "beams". These beams are directed toward a substrate surface, where they deposit material that forms crystal structures. The growth rate of these crystals is very low, typically on the order of a third of a monolayer per second, which allows for very fine interface control.

The main chamber of an MBE is kept under UHV through the use of an ion pump and a cryo shroud. In MBEs that do not contain phosphorus, a cryo pump is used as well. The cryo shroud is simply a shell inside the outer wall of the MBE that has liquid nitrogen (LN2) circulating through it to cool it down to 80K. Since this shroud is cold, stray particles that hit it will stick to it, thereby having a pumping effect on the chamber. This, combined with an ion and cryo pump, allows the MBE to get to pressures on the order of 10^{-10} Torr. The drawback is that MBE machines use a considerable amount of LN2 to maintain the cryo shroud temperatures, which can become costly given the 24/7 need to maintain the flow of LN2 through the shroud.

2.5.3 MBE Materials

The material in an MBE system is required to be very high purity. The material used is typically in the range of 7N, or 99.99999% pure (seven total 9s, hence the 7N designation). These materials are stored in crucibles made from pyrolytic boron nitride (PBN), which is a ceramic material that is capable of withstanding temperatures up to roughly 1600°C. These crucibles come in a variety of designs, most commonly in cylindrical, conical, and SUMO® cell designs. The design of crucible used in the cell depends heavily on the degree of stability required and, as is true in many things, the available budget. For the purposes of this dissertation, III-V materials including

Al, Ga, In, As, and Sb, will be the focus of discussion. Each of these cells are water cooled to prevent crosstalk (heating of adjacent cells). Furthermore, each cell has an associated shutter that can be open or closed relatively quickly (sub-second timing) to begin or end material growth abruptly. This allows for very fine interfaces to be created.

Group-III Materials

The PBN crucibles are housed inside effusion cells (also called Knudsen cells). The crucible itself is surrounded by a vertical coil of heater wires. For group-III materials, the heater coil is generally segmented into two zones, a tip and a base. This is done to prevent spitting, which is when a small bit of material shoots out of the crucible and sticks to the surface of the substrate, thereby creating a large defect in the device. Gallium typically has an issue with spitting that can be mitigated by maintaining a tip temperature considerably higher than that of the base (where the material itself resides). Indium also shows this issue to a lesser degree.

Aluminum, however, has a much different problem. Over time, aluminum will show a tendency to "creep" up the sidewalls of the PBN crucible. This will naturally cause undesired variation in the growth rate, and can result in aluminum actually leaving the crucible and shorting the surrounding heater wires. In order to prevent this, the tip of the aluminum cell is kept cooler than the base of the cell. This causes the creeping aluminum to effectively stop on the tip of the cell, thereby preventing any aluminum from damaging the cell.

The temperature of the base of each group-III cell is used to control the amount of material coming out of that cell. Since most III-V growth is done under group-V rich conditions (where excess group-V material is provided to the substrate surface), this will also control the material growth rate. In order to calibrate this growth rate,

a technique called reflection high-energy electron diffraction (RHEED) is used.

RHEED

The RHEED technique relies on impinging high energy electrons on a sample surface to obtain information as to the quality of that surface. This technique uses an electron gun, which contains an emissive filament and electron optics that are able to focus and direct the emitted electron beam onto the sample surface. The beam reflected off this surface is detected by a phosphorus-coated leaded-glass window. The results show up as bright spots on the screen. These spots will form a pattern depending on the material in question and the rotation angle of the substrate. III-V materials will typically have two distinct patterns that can be seen by varying the rotation angle. These patterns are separated from one another by 90°. A RHEED pattern is characterized by bright spots separated by dimmer lines. The convention for describing a RHEED pattern is to count the number of dark spaces that reside between two bright spots, where the dark spaces exists between the dimmer lines. Crystalline GaSb heated to growth temperatures will exhibit a 1x3 (one by three) pattern, for instance, which means the RHEED pattern will simply have dark space between two bright spots at one angle, and two dimmer lines between bright spots (and thus three dark areas) at an angle 90° off from the 1x (one by) pattern. A 3x pattern is shown in figure 2.2.

The reason that III-V RHEED patterns emerge is related to the surface of the crystalline substrate. If one were able to perform RHEED on a layer below the surface, a pattern called a 1x1 would emerge. Typically, these surfaces are group-V rich, so the RHEED pattern will be related to the group-V atoms. In every layer beneath the surface, the group-V atoms will be bonded to the group-III atoms that are directly above and below them. However, on the surface of the sample, there are no group-III atoms above to bond to, so the group-V atoms effectively bond to

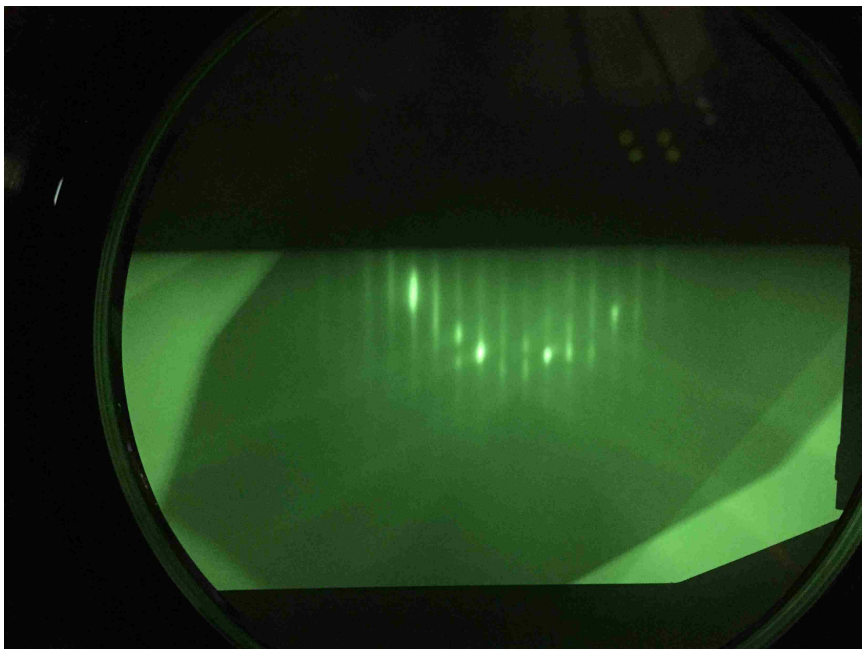

Figure 2.2: An image of a 3x pattern from GaSb RHEED. The 3x (3 by) name comes from the number of dark spaces between each pair of bright spots.

each other. In order to do this, they move towards each other. Due to the bonds with the group-III atoms below them, these group-V atoms are restricted in the [110] plane. However, they are able to move along the [-110] plane, which is 90° off from [110]. By moving as they do, the unit cell of the crystal lattice, which is the smallest pattern that can be repeated to re-create the full crystal, changes. If these atoms did not move, a 1x1 pattern would form, since the surface would be comprised of squares. However, due to the movement along one direction, the "square" pattern is maintained along the [110] direction but not along the [-110] direction, thus resulting in the 1x3 pattern exhibited by GaSb, for example. For GaSb in particular, the 3x portion of the pattern will visibly change to a 5x pattern at a surface temperature of roughly 400°C. The pattern will change back from 5x to 3x at roughly 420°C, which can be useful for determining growth temperatures when a pyrometer measurement is not available.

Another use for RHEED is in the calibration of growth rates for the group-III cells. Since RHEED involves reflection, the bright spots will dim somewhat when the surface becomes rough (or vanish entirely if the roughness is bad enough). This roughness occurs during the growth of a single monolayer. During the growth of a single monolayer, the material will slowly deposit on the surface of the sample and form islands (partial layers). As growth continues, these islands will begin to merge together until a complete monolayer is formed. RHEED is sensitive enough to detect this process occurring. By stopping substrate rotation and focusing on a single bright spot, the intensity of the spot can be monitored. Over the course of growth for a single monolayer, this intensity will gradually decrease until the monolayer is half-grown, then begin to increase again (reaching a maximum when the monolayer is complete). By observing the growth of several monolayers, the frequency of the intensity peaks can be observed. The growth rate is then equal to the frequency of the effective sinusoid generated by the oscillating peak intensity. An example of this sinusoid is shown in figure 2.3.

By observing the growth rate at several different cell base temperatures, an Arrhenius plot can be created. This is done using the cell temperature in Kelvin and the log of the growth rate, and, presuming the cell is operating correctly, will result in the points forming a straight line, as shown in figure 2.4. This line can then be used to extrapolate the cell temperature needed to achieve a specific growth rate. Also, the growth rate on different materials can be determined simply by multiplying by the squared result of the desired material lattice constant divided by the lattice constant of the material (typically GaAs or InAs) used to obtain the initial growth rate.

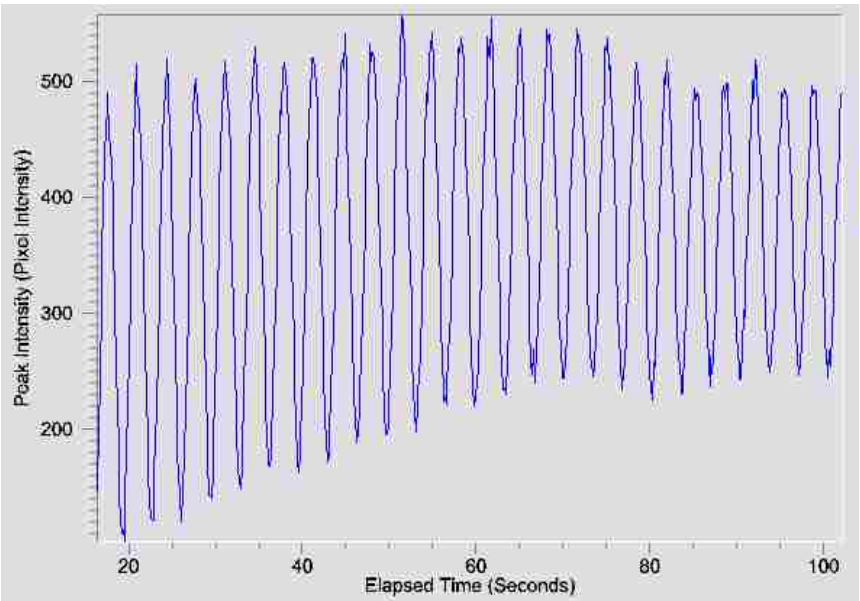

Figure 2.3: RHEED spot intensity plotted vs. time. The period of this sinusoid is equal to the growth rate of the material. This image is taken from a kSA 400 system [63].

Group-V Materials

The group V cells (As and Sb in this case) are designed in a different manner from the group III cells. An MBE machine growing under group-V rich conditions, as most do, will typically store considerably more group V material than group III material. Furthermore, the group V sources provide tetramer material (As_4 and Sb_4). By splitting these materials into dimers, the growth conditions required to produce high quality material are extended, thereby providing a larger range of acceptable conditions. In order to accomplish this, the group V cells are designed effectively as a bottle with a long neck that is heated to (typically) 900°C. The base of these crucibles is separate from the cracking zone, and is used to control the amount of material (flux) coming out of the cell. When the group V atoms pass through this hot zone, called a cracking zone, they are split into dimers, which then exit the cell and travel to the substrate surface. In some cases, the cracking zone may contain a

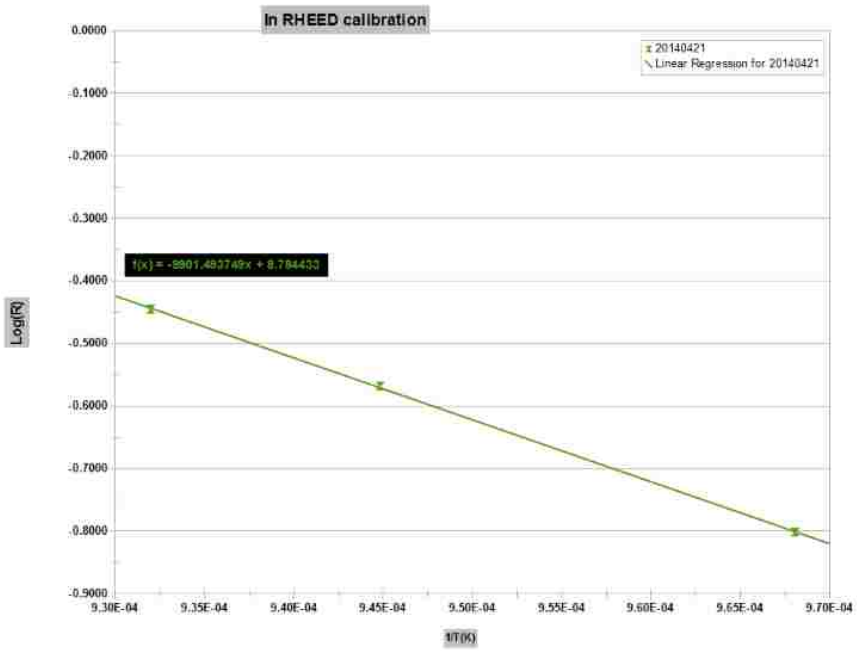

Figure 2.4: Arrhenius plot of the growth rate versus 1 / (cell base temperature). By plotting the logarithm of the growth rate, a linear fit can be made to the points, thereby providing a method for calculating the cell temperature required to reach a specified growth rate.

needle valve. This removes the need to vary the temperature of the bulk material, and allows for relatively fine control of the flux coming out of the cell. This also improves the stability of the source, since the bulk does not need to be heated prior to and cooled after each growth, but instead can maintain a constant temperature. This is particularly helpful when growing materials that contain both As and Sb, such as in the Ga-free SL.

2.5.4 Doping

The doping level in a material can be an important factor to control. In order to do that, the dopant cell temperature is varied based on the level of doping required. The cell temperature is determined through a series of doping calibration samples. The

requirements of these samples depends on the method used to measure the doping level. This thesis will focus on using Hall measurements to determine doping levels.

In order to perform accurate Hall measurements on a sample, a semi-insulating GaAs substrate is used. This is necessary to ensure that doping in the substrate does not affect the reading from the doped epilayer. The epilayers of the samples are doped GaAs, where the dopant cell temperature is different for each sample. The thickness of this epilayer is somewhat dependent on the level of doping present. For higher levels of doping, on the order of 10^{16} or higher, 2μm will prove to be more than enough. However, for low doping levels or background doping measurements, thicker samples are required. These will typically require an epilayer thickness of 5μm. This is to ensure that the sample thickness is greater than the depletion width of the doped material, since the substrate can interfere with the measurement results if this is not the case.

In the case of a background doping measurement, the GaAs epilayer is not intentionally doped, meaning the dopant cell is left at idle temperatures, and the dopant cell shutter remains closed throughout the growth. This is done to determine the level of doping induced by material in the MBE growth chamber. This value will typically be in the 10^{14} to low 10^{15} cm^{-3} range. In order to achieve lower background doping levels, any heated filaments, such as pressure gages, should be turned off during growth. This is due to the fact that heated filaments will emit a very small amount of material that can incorporate into growth. For reference, the background doping level in CHTM's Gen10 MBE was measured to be $1 \cdot 15$ cm^{-3} with the chamber BEP and flux gauge turned on (where these are Bayard-Alpert nude filament gages), and $1 \cdot 10^{14}$ cm^{-3} with the gauges off.

Once the calibration samples are grown, the doping level can be measured using a Hall measurement setup. This will provide numbers for the doping of each sample. These results can be fitted by a line using an Arrhenius plot, which is log(Doping) vs.

1/CellTemperatureInKelvin. The equation of this line can then be used to calculate the cell temperature required for a desired doping level. This process is the same as that used to determine the group-III cell growth rates.

2.5.5 X-Ray Diffraction

The primary method for determining the quality of a grown crystal structure is single-crystal high-resolution x-ray diffraction (XRD). This method uses the periodicity present in the single crystal to analyze the crystalline structure of the device. In this case, the crystal is illuminated by x-rays, which then diffract off the atoms present in the material. Due to the regularity of the atoms, this causes a pattern of constructive and destructive interference based on the angle of incidence. In single-crystal XRD, an $\Omega - 2\theta$ scan is used. This produces a scan that can be used to determine the properties of a crystalline structure. One such scan is seen in figure 2.5. The constructive interference in an XRD scan is defined by Bragg's law, which is as follows:

$$d = \frac{n\lambda}{2sin(\theta)} \tag{2.9}$$

The separation between the main epitaxial peak and the substrate peak indicates the degree of mismatch present between the epitaxial and substrate crystal lattice constants. To be considered lattice matched, this angular peak separation must be less than 100 arcseconds (conventionally). The angular peak separation can be translated directly into a percentage lattice mismatch, expressed as $\Delta a/a$ by calculating each lattice constant using the measured XRD peaks and Bragg's law. The relevant equation for this calculation is:

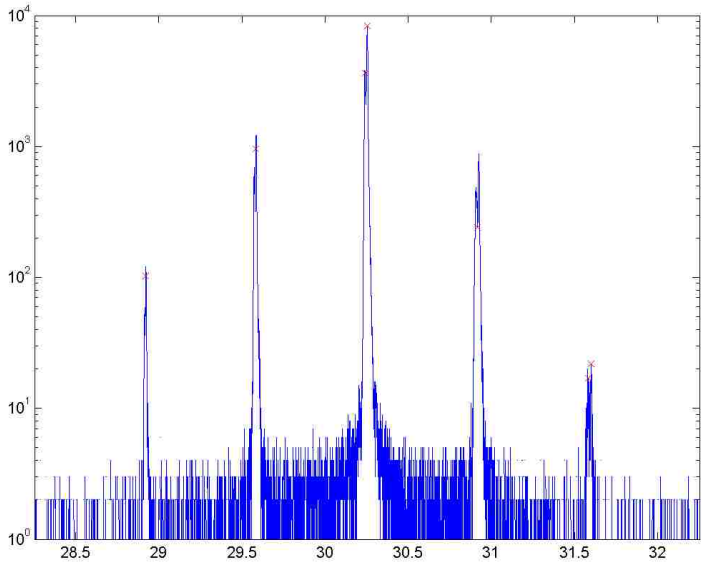

Figure 2.5: An example of an XRD scan (004) of a superlattice structure. In this scan, multiple distinct peaks can be seen. The tallest peak in this case is the 0^{th} order peak for the SL, with 1^{st} and 2^{nd} order peak pairs. The substrate peak can be seen near the 0^{th} order peak, indicating that the sample is very slightly (49 arcsec) off perfect lattice match.

$$\Delta a/a = \frac{d_{0th} - d_{substrate}}{d_{substrate}} \tag{2.10}$$

Which can be simplified through some algebra to the following equation [64]:

$$\Delta a/a = \frac{sin(\theta_{substrate})}{sin(\theta_{substrate} + \Delta\theta)} - 1 \tag{2.11}$$

It should be noted that this process does not calculate the strain in the system, only the degree of lattice mismatch as measured by XRD. In the case of SL materials, the SL period can be determined using a similar process. In this case, the 1^{st} order

peaks on either side of the main peak are used. The relevant equation in this case can be simplified to:

$$\frac{\lambda}{sin(\theta_{R1}) - sin(\theta_{L1})} \tag{2.12}$$

where λ is the wavelength of the XRD source ($1.54056\mu m$ for the $Cu - K\alpha_1$ line commonly used in single crystal XRD), and the two angles are for the right and left side 1^{st} order diffraction peaks.

2.5.6 Ga-free Superlattice Material Growth

Growth of the Ga-free SL material can often prove problematic, particularly due to the presence of InAsSb. A desired composition of InAsSb will be difficult to obtain and maintain due to the intrinsic difficulties in group-V intermixing. This can also smear the superlattice interfaces, and is particularly evident on the InAs-on-InAsSb interface [44]. Since the group V materials are provided in excess, the composition cannot simply be determined by setting the material growth rates to the correct ratio. Instead, the BEPs of the two sources (As and Sb) must be set to achieve the correct composition. However, it is not as simple as setting the BEP ratios to match the desired composition due to the varying incorporation ratio based on the growth conditions. Instead, the growth conditions must be calibrated via growing a test sample, checking the lattice mismatch using XRD, then adjusting the source BEPs as needed. In order for this to work correctly, the growth temperature must also be consistent, as the InAsSb composition in the Ga-free SL is highly dependent on growth temperature[65, 66, 67]. This is visualized in figure 2.6 [57].

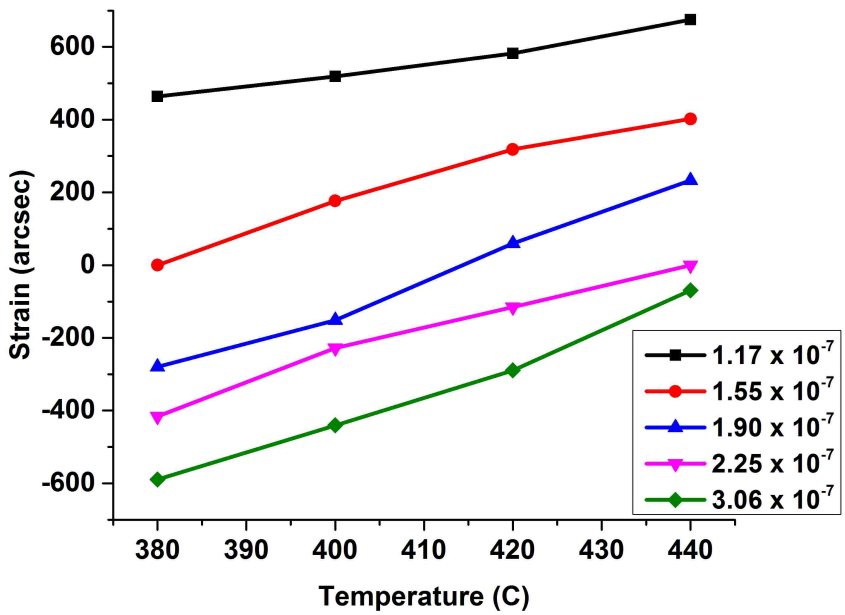

Figure 2.6: Angular difference between substrate peak and epitaxial peak as measured by XRD for a series of 14ML InAs- 12ML InAsSb SLs grown at different growth temperatures and using varied Sb BEPs. For this graph, the growth rate and As BEP were kept constant. [57]

2.5.7 Modulated MBE

Modulated MBE (MMBE) was developed as a tool to alleviate the strong compositional dependence of mixed group V materials (such as InAsSb) on growth temperature and source BEP. This alleviation is accomplished by controlling the composition through shutter timings rather than through the ratio of group V BEPs. Alternating the shutters results in the formation of thin regions of binary material, which theoretically will behave the same way as a random-alloy ternary. The reduction in dependence on temperature and BEPs has been demonstrated in literature [68, 69, 70]. For the Ga-free SL, this would mean a marked improvement in growth stability and repeatability, which is highly desirable for both research and production purposes. Improved crystalline quality in the Ga-free SL obtained through the use of the MMBE technique has been demonstrated previously [44, 45, 71, 72]. The

viability of using this technique to create an IR detector is the subject of one of the later chapters in this dissertation.

Chapter 3

Baseline Homojunction Device

The first steps taken toward producing a MWIR Ga-free SL-based photodetector required an initial design that would indicate the layer thicknesses required to obtain MWIR performance. This was done using an empirical pseudopotential method (EPM) model created previously for InAs-GaSb SLs [35, 73, 74], and modified to work for the Ga-free SL. The initial simulation showed that the 14ML InAs - 12ML $InAs_{0.65}Sb_{0.35}$ superlattice would provide an MWIR cutoff predicted to be at 5μm. The band lineup of the two materials obtained through the simulation can be seen in figure 3.1 [58]. Since the EPM simulation requires tuning through the use of empirical data, the expectation was that the initial devices would not exhibit the exact cutoff wavelength for which they were designed.

One issue with this particular design is that the composition of the $InAs_{0.65}Sb_{0.35}$ layer at the given 14ML InAs and 12ML InAsSb layer thicknesses does not result in a superlattice that is perfectly lattice matched to the GaSb substrate on which the material is grown. An HRXRD analysis of the resulting device showed a 500 arc-second compressive mismatch, which can be seen in figure 3.2. A room temperature photoluminescence measurement taken from the grown structure indicated a cutoff

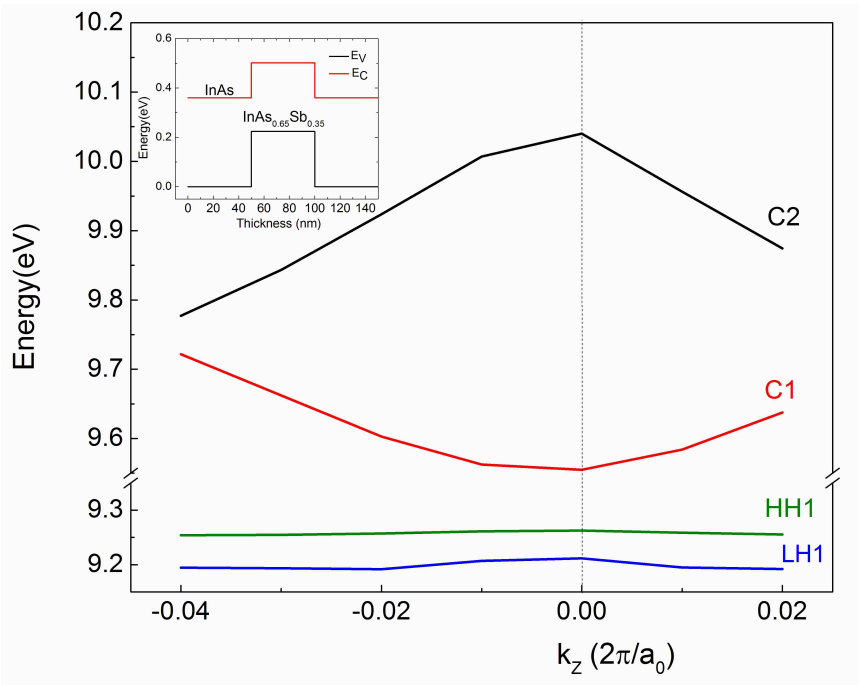

Figure 3.1: The results of the EPM simulation of a 14ML InAs - 12 ML $InAs_{0.65}Sb_{0.35}$ SL. The main figure shows the conduction (C1, C2) and valence (HH, LH) band energies of the superlattice, and the inset of the figure shows the band lineup of these two materials. [58]

wavelength above 5.5μm [58]. The 5.5μm in this measurement is a limit of the InSb detector used in the setup, not a property of the device itself.

The sample described here was grown in a Veeco Gen10 MBE as part of a series of three samples meant to determine the optimal growth temperature for the Ga-free SL. This series included growths at substrate temperatures of 380, 400, and 420°C. However, the growths at 380°C and 400°C did not produce working devices, whereas the growth at 420°C did. The dependence of InAsSb composition on growth temperature was accounted for by varying the Sb source BEP to create the desired As/Sb ratio. Sub-optimal growth temperatures have been shown to increase the dark current [35], which is due to an increase in defects present in the device. These defects have been attributed to group V accumulation at lower growth temperatures and

group V diffusion across SL interfaces at higher growth temperatures [10]. Elevated growth temperatures can also result in behavior similar to an insufficient group V flux. For superlattices, killer defects primarily occur at the interface between the GaSb buffer layer and the SL, and are associated with elevated growth temperatures [75]. The Sb accumulation seen at lower substrate temperatures can also occur during oxide desorption on GaSb substrates [76]. Current in-progress research is demonstrating that these Sb-clusters can have a very detrimental effect on device performance. For the Ga-free SLs, which have a small amount of Sb, some clustering of Sb atoms may occur, thereby inducing defects in the crystal. Additionally, As can form antisite defects at lower growth temperatures, that will also negatively affect device performance[77]. In the case of growth temperature, erring in either direction results in increased defect densities. In the case of these samples, this increased defect density combined with the already high dark current exhibited by the working device is currently theorized to have resulted in the poor performance of the detectors grown below 420°C. This was used to determine the 420°C growth temperature that has been used throughout this dissertation for Ga-free samples.

The structure used for this initial device was a PIN design, with contacts doped at $4 \cdot 10^{18}$ cm^{-3}, using Be for the p-contact and Te for the n-contact. The doping in these contacts was graded over 10 periods by raising the dopant source temperature while the dopant source shutter was opened. The absorber in this sample was not intentionally doped (n.i.d.). The layer thicknesses were 0.5μm for the n-contact layer, 1μm for the absorber, and 80nm for the p-contact. The thick n-contact is based on processing concerns. Since the n-contact is the bottom layer, an etch is required to reach it. This etch can have some variance in depth, so a reasonably thick layer is preferred to ensure that the bottom contacts of the devices are all actually in this layer, rather than in the substrate below it or the intrinsic layer above it. This structure is illustrated in figure 3.3[57].

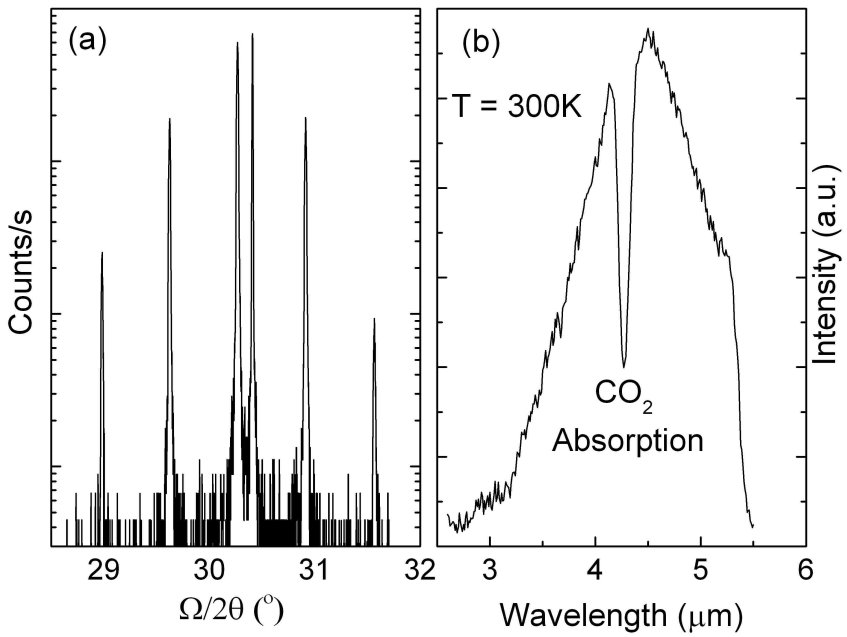

Figure 3.2: The HRXRD analysis of the initial Ga-free PIN sample, shown on the left, indicates that the epitaxial layer is compressively mismatched by 500 arcseconds on the GaSb substrate. The photoluminescence measurement performed on the sample, shown on the right, indicates a cutoff wavelength greater than that of the InSb detector used in the setup (5.5μm).[58]

After these initial measurements, this sample was processed into a series of 410 x 410μm square mesas through the use of a tartaric acid etch. The top and bottom device contacts were deposited on the etched sample using Ti/Pt/Au. The top contact for these devices defined circular apertures of varying diameters on the etched mesas. The device was finalized with a SiN_x passivation layer. An example image of the mesa designs can be seen in figure 3.4.

The processed devices were characterized for dark current, spectral response, and quantum efficiency. The spectral response demonstrated by the devices showed a 77K 50% cutoff wavelength of 5.4μm, and a 100% cutoff at roughly 6μm. This is shown in figure 3.5 [58]. This data point was used to tune the EPM simulation. The

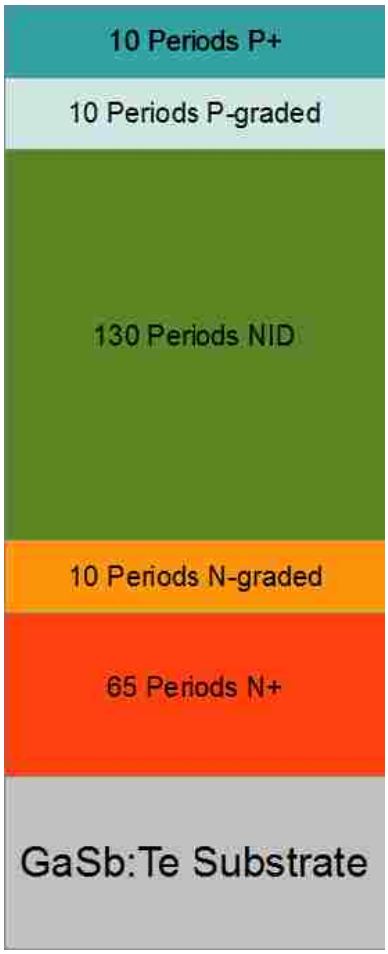

Figure 3.3: A diagram of the structure grown for the initial Ga-free SL PIN photodiode.[57]

quantum efficiency of this device was measured to be roughly 20% under a -10mV bias voltage at 77K.

The dark current of this device was also measured, and was surprisingly high given the lifetime reported in literature. This may in part be due to the lattice mismatch present in the device. The results of the dark current measurements are shown in figure 3.6. An Arrhenius plot of the dark current is shown in figure 3.7.

The dark current characteristics of this device were analyzed using a modified

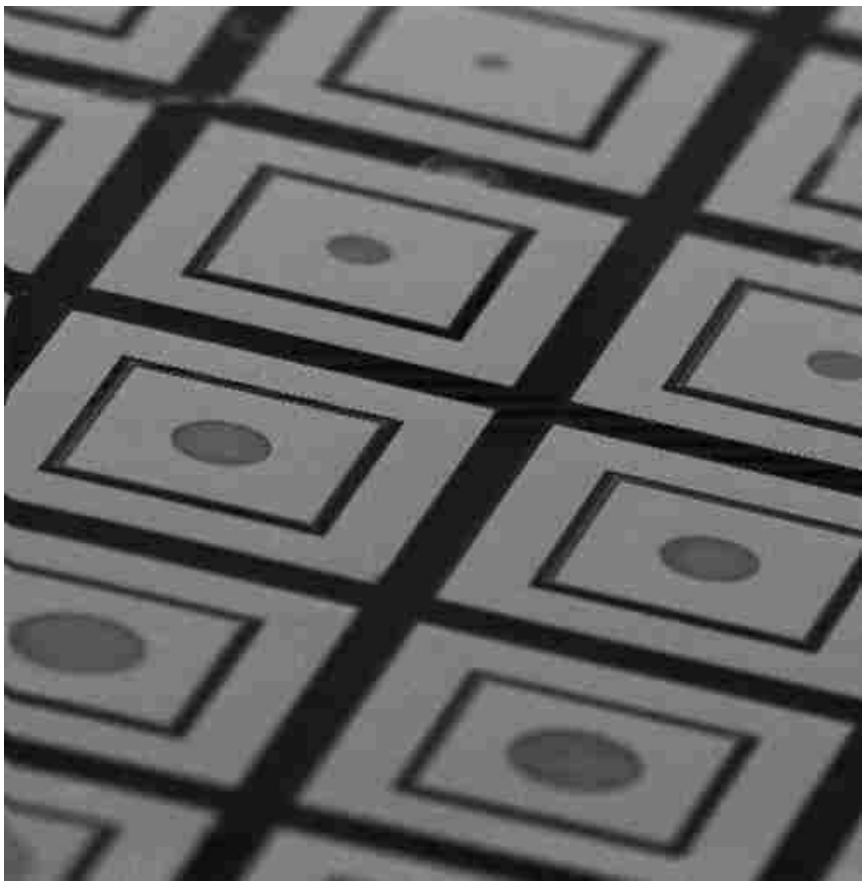

Figure 3.4: An SEM image of a processed series of devices. The bottom contact of each etched mesa can be seen surrounding the mesa itself. The top contacts on each mesa define a circular aperture that varies in size from row to row.

version of a program provided by IR Nova[78]. This program works to fit the dark current of the device to a combination of diffusion, G-R, and trap assisted tunneling (TAT) dark currents based on the characteristic curve shapes of each type of dark current. The fitting parameters include the current amplitude and, in the case of BTB and TAT, a rate term in an exponent. This is based on a modeling method described for MCT detectors[79]. The results of this are shown in figure 3.8. This indicates that TAT may be playing a role in the observed dark current. Defects are particularly likely to form at the interface between the GaSb buffer and the

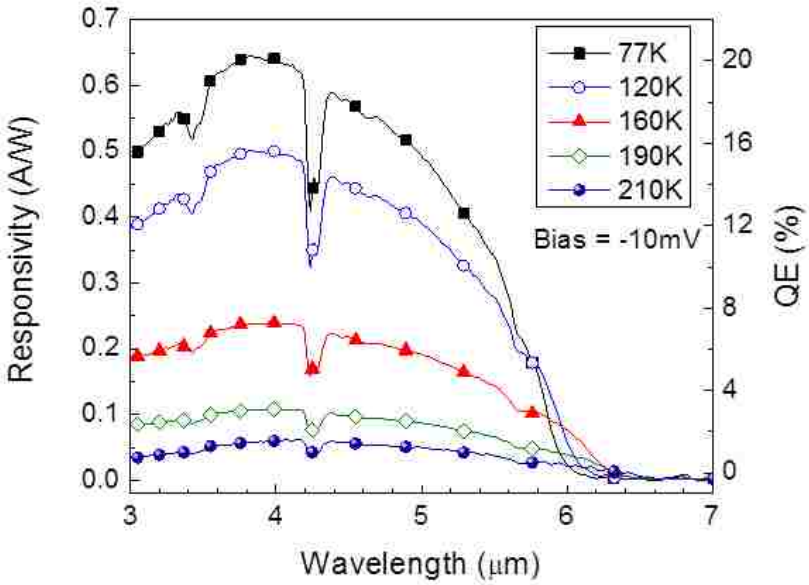

Figure 3.5: Spectral response of the initial PIN structure Ga-free photodiode. This shows a 100% cutoff wavelength at 77K of roughly 6μm.[58]

subsequent superlattice layers under suboptimal growth conditions [75], so optimizing the growth and thereby reducing the density of these defects is expected to improve the dark current levels in future devices.

In conclusion, an MWIR Ga-free SL-based PIN detector was grown. Electrical characterizations were performed on the resulting devices, which demonstrated a dark current level considerably higher than would be expected from the drastically improved carrier lifetime over that in the InAs-GaSb SL. These were the first reported electrical characterizations (dark current and quantum efficiency) for a Ga-free SL detector. Some initial modeling indicated that the dark current may be dominated by the trap-assisted tunneling process. The rest of this dissertation focuses on reducing the levels of dark current present in Ga-free SL PIN detectors.

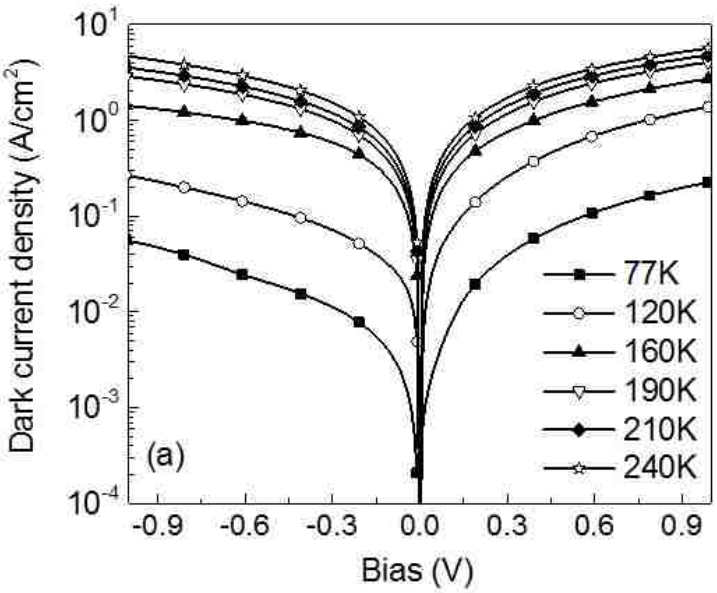

Figure 3.6: Dark current vs. bias voltage and temperature for the initial Ga-free PIN photodiode.

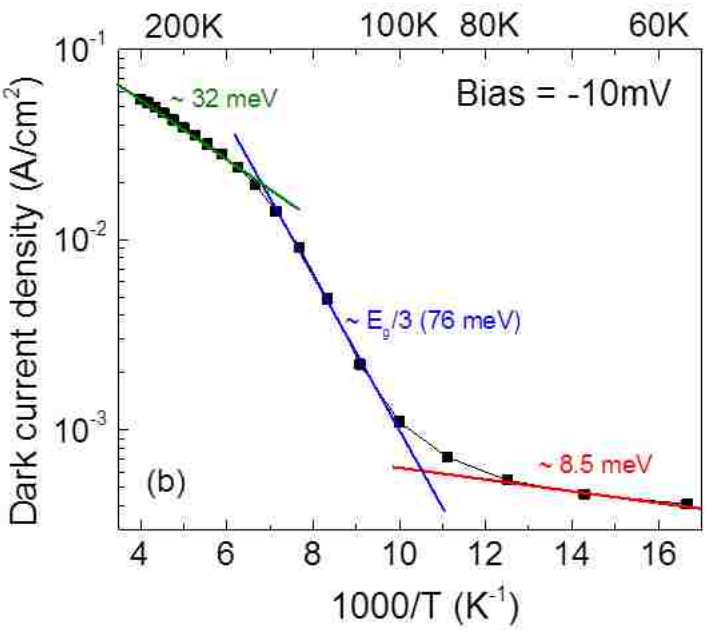

Figure 3.7: The temperature-dependent dark current densities measured at a bias of -10mV. The activation energies of each portion of the curve are also shown.

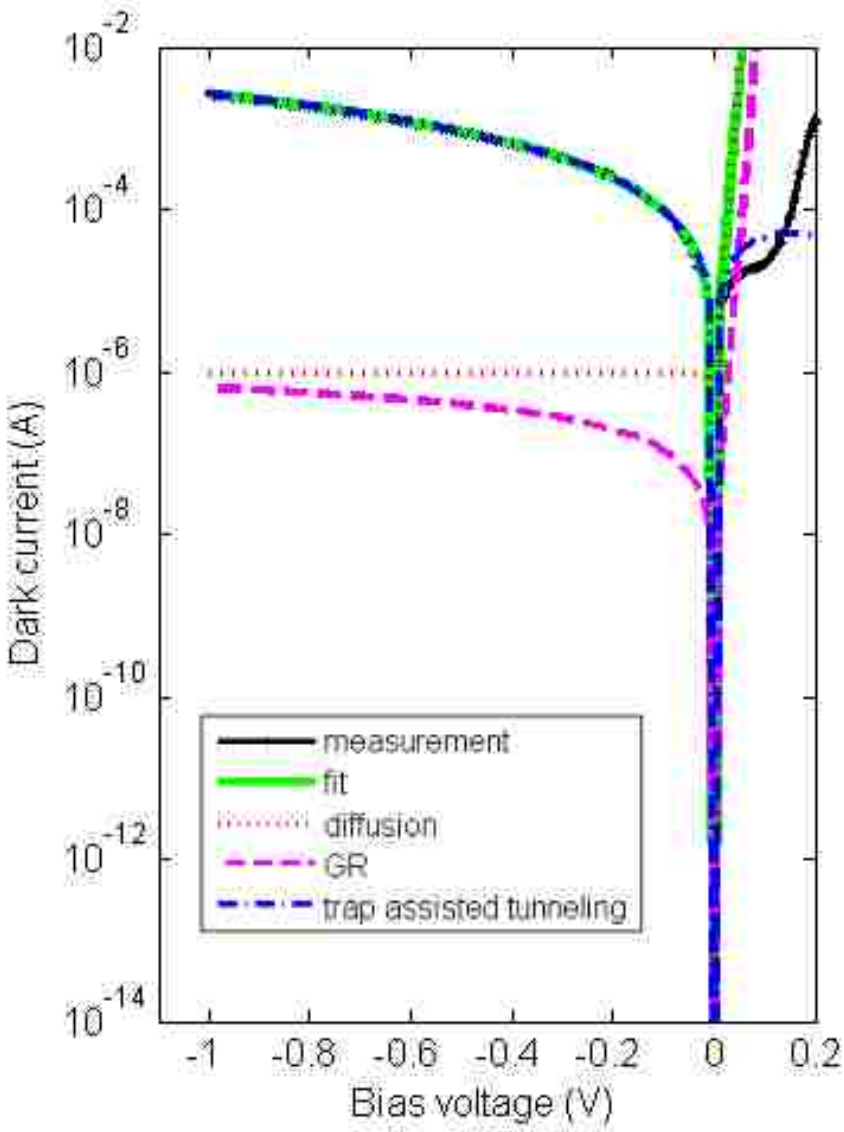

Figure 3.8: The results of the IR Nova dark current fitting program. This shows a high degree of TAT to be the source of the high level of dark current present in the device.[57]

Chapter 4

Absorber Doping in Ga-free SLs

The results of the initial device showed a relatively high level of dark current in spite of the predicted reduction given by carrier lifetime studies. This was assumed to be in part due to the lack of optimization studies on the growth of Ga-free devices. To that end, several optimization studies were planned in order to reduce the dark current levels in future devices. The first of these studies was to test the effect of a light p-type doping in the absorber layer of PIN structure Ga-free SL-based devices.

The motivation behind this study arises from the fact that InAs, which is the primary constituent material of the Ga-free SL, is intrinsically n-type [80]. Previous studies performed on an InAs-GaSb SL with a thicker InAs layer demonstrated a reduction in dark current and an improvement in quantum efficiency when the intrinsic n-type properties of the SL were compensated with a p-type doping [81]. In order to test whether this proved to be true for the Ga-free SL, a series of PIN structures were grown with varied p-type compensation doping in the absorber layer.

These samples followed the groundwork laid by the initial device, though the design of the superlattice was altered slightly. For these devices, the superlattice was a 14ML InAs - 12ML $InAs_{0.81}Sb0.19$ superlattice, which has a different InAsSb

composition from the first device. This design was meant to be lattice matched to GaSb, thereby eliminating the lattice mismatch present previously. Also, it was meant to shift the bandgap of the material from close to 6μm down to roughly 5μm, which was more in line with the intended parameters. The reason behind this change in design was due to a shift in the parameters of the EPM simulation used to design the SL. The material parameters present in the simulation were adjusted after the results of the initial devices to ensure that the simulated material demonstrated the same bandgap as the grown device. After this adjustment, the simulation was re-run to find a superlattice composition that would provide the desired 80K 5μm cutoff wavelength.

The samples themselves were PIN structure devices, with contact regions doped at $2 \cdot 10^{18}$ cm^{-3} using Be for the p-contact and Te for the n-contact. This was reduced from the initial device in order to bring the contact dopings more in line with the doping levels used in InAs-GaSb devices. There was also some initial concern over defects induced from the high levels of doping, though this has not been definitively demonstrated. It would be prudent to conduct future studies on the optimal contact doping levels in these devices, but this has not been done in this dissertation. The thicknesses of the contact layers were 500nm (n-contact) and 80nm (p-contact). The absorber layer was 2μm thick, and was doped differently for each sample. The thickness of the absorber region was increased from the initial device in order to increase the resulting device quantum efficiency. The dopings used included an NID reference sample, $5 \cdot 10^{15}$, $1 \cdot 10^{16}$, and $3 \cdot 10^{16}$ cm^{-3}. These doping levels were determined using the procedure described in section 2.5.4. The background doping level of the MBE chamber was measured to be $1 \cdot 10^{15}$ cm^{-3}. The lowest absorber doping level was selected to be above this level. The samples were grown at 420°C (measured by pyrometer). XRD measurements were performed on the grown samples. The results are shown in figure 4.1[57]. The slight compressive lattice mismatch shown in the figure indicates an InAsSb composition of $InAs_{0.781}Sb_{0.219}$. The expected cutoff

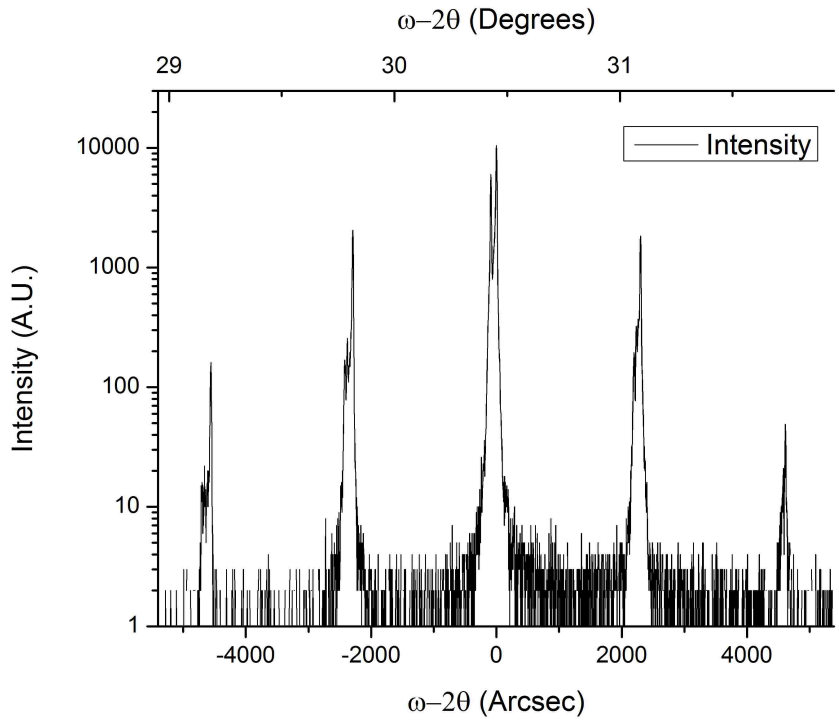

Figure 4.1: Representative XRD of the grown samples from the doping study. From this figure, a slight compressive mismatch can be seen. This was calculated to be a mismatch of 0.082%, which translates to an $InAs_xSb_{1-x}$ composition of x=21.9%. [57]

wavelength at 80K calculated from the EPM simulation using the new composition is 5.26μm.

The grown devices were processed similarly to the initial device, though a different mesa mask was used. In this case, the mesas were circular, with sizes ranging from 25 up to 400μm in diameter. The resulting devices were characterized at the Air Force Research Laboratory on Kirtland Air Force Base in Albuquerque, NM. The spectral response is shown in figure 4.2. The 80K 100% cutoff wavelength at 5.2μm indicates that the EPM simulation is accurate.

The resulting dark current measurements from the best devices from each sample are shown in figure 4.3. Both the best devices and average dark current values are

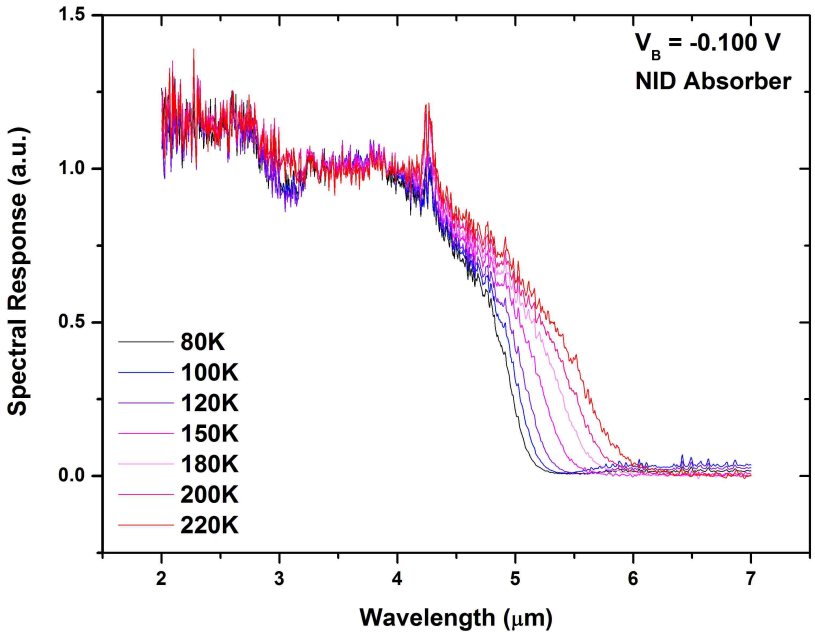

Figure 4.2: Representative spectral response for the doping study samples. This shows a cutoff wavelength of roughly 5.2μm at 80K, which is in agreement with the EPM simulation.[57]

compared in figure 4.1. The dark current levels indicate that the highest doping level tested, at $3 \cdot 10^{16}$ cm^{-3} resulted in the best performance. This result is in agreement with the assumption that the carrier concentration in the intrinsic region is dropping due to the compensation doping. According to more recent research, this should occur up to $5 \cdot 10^{16}$ cm^{-3} doping [82]. The dark currents from these devices at high bias show a sharp increase, which is currently attributed to impurities present in the passivation layer used during the processing. Due to the design of the particular mask used to generate the mesa contacts, the connection to the top contact of the devices is made to a contact pad connected to a metal contact on the top of the mesa, rather than directly to the top of the mesa itself. This pad is placed on top of the passivation layer, so impurities between the contact pad and the bottom contact layer could be causing an increase in the measured current at higher biases.

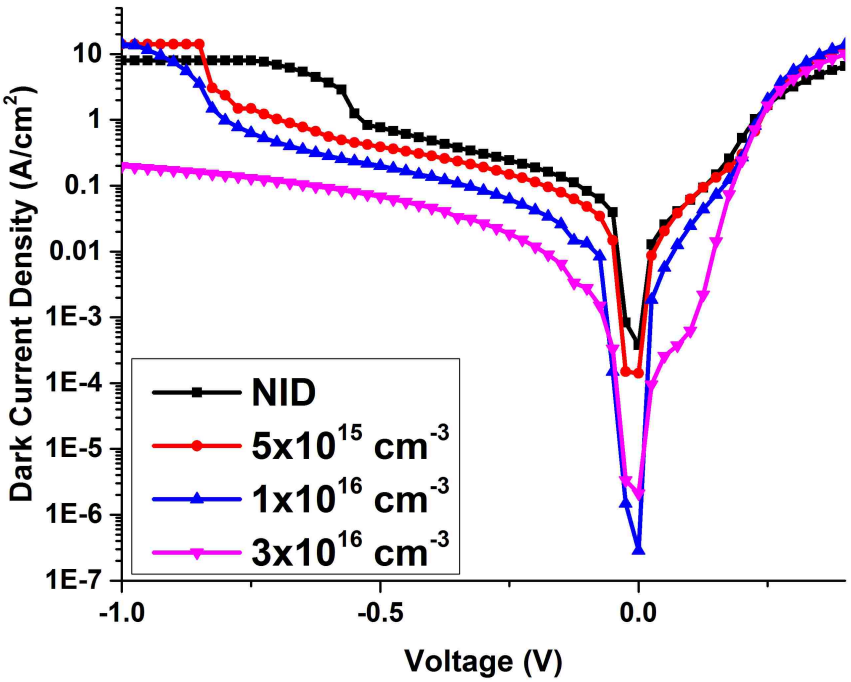

Figure 4.3: A comparison of the dark currents resulting from the best devices from each sample. This indicates that the highest p-type doping level tested resulted in the lowest dark current.[57]

The final piece of characterization needed was the quantum efficiency. In order to measure this, photocurrent measurements were performed on each device. These measurements are shown in figure 4.4.

From the results, the quantum efficiency was calculated, and is reported for each device in figure 4.1. The results from the quantum efficiency measurements indicate a slight trend downward with the increase in doping. The $1 \cdot 10^{16}$ cm^{-3} sample shows a sharp decrease. There is some uncertainty in these measurements due to the variance between different devices, so the results indicate primarily that the devices (other than the one outlier) are similar in QE. The improvement in the quantum efficiency in these devices is due to the increased thickness of the absorber region. There is evidence in literature that increasing the doping level further will continue to improve device performance [82], so continuation of this experiment via higher doping levels

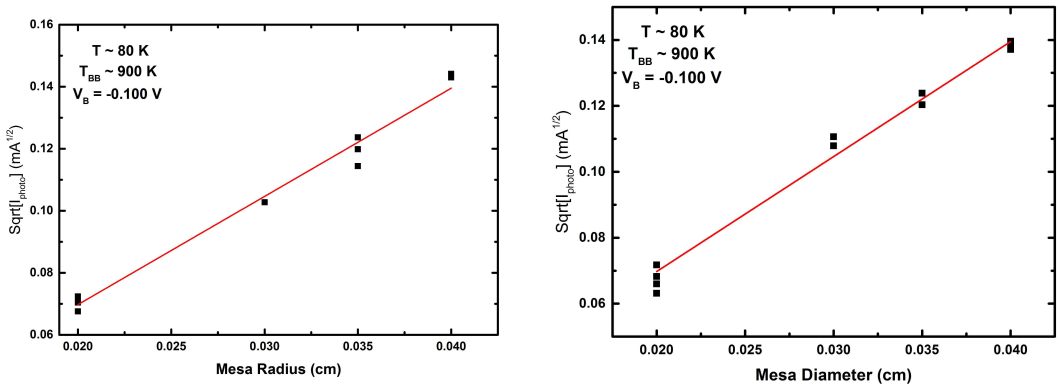

(a) NID (b) $5 \cdot 10^{15}$

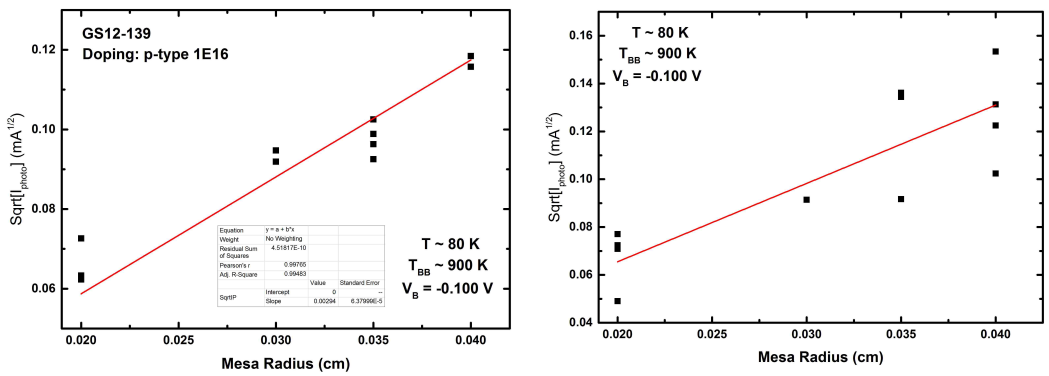

(c) $1 \cdot 10^{16}$ (d) $3 \cdot 10^{16}$

Figure 4.4: Photocurrent results from the doping study samples. The results are taken from varied aperture diameter devices from each doping level.

is encouraged. The dependence of dark current on doping level is shown in figure 4.5, which shows that the improvement from p-type doping begins to level off above $1 \cdot 10^{16}$ cm^{-3}. Unlike the study conducted on the InAs-GaSb device, the QE in the Ga-free SL devices does not increase with the doping.

Absorber Doping	Average Dark Current (A/cm^2)	Best Device Dark Current (A/cm^2)	Quantum Efficiency
N.I.D. (-0.1V, 80K)	0.2055	0.08353	42.4
$5 \cdot 10^{15}$ (-0.1V, 80K)	0.0912	0.03266	42.1
$1 \cdot 10^{16}$ (-0.1V, 80K)	0.0689	0.01338	30.1
$3 \cdot 10^{16}$ (-0.1V, 80K)	0.0488	0.00248	37.4

Table 4.1: A table compiling the results of the doping study. All doping levels here are p-type. The results here indicate that a $3 \cdot 10^{16}$ cm^{-3} doping in the absorber layer produced the best results. The data here was taken at 80K and a bias voltage of -0.1V.[57]

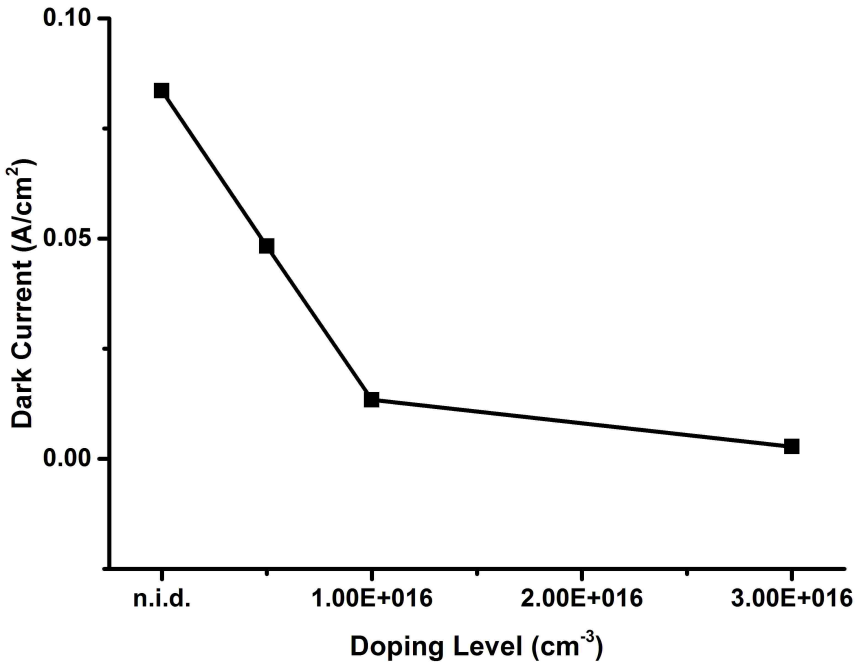

Figure 4.5: Dark current density plotted vs. doping for the best devices from each sample. The approximate linearity existing from n.i.d. to $1 \cdot 10^{16}$ matches expectations from the given G-R equation. The switch from n-type to p-type occurs roughly at $3 \cdot 10^{16}$[82], which causes the linearity to no longer hold.[57]

Chapter 5

As:In BEP Ratio effects on Ga-free SL Growth

Another important consideration in any growth is the ratio of group V to group III present during growth. This is typically referred to as the flux ratio or BEP ratio, depending on what is measured. In most MBE machines, a pressure gauge is used to determine the amount of material coming out of a cell. This is the Beam Equivalent Pressure (BEP) measurement. This measurement is distinct from the actual flux, since flux is a direct determination of the amount of material reaching the surface of the sample. Due to this, BEP ratios and flux ratios for the same growth conditions will be different. For this study, BEP ratios will be used.

In order to grow high quality material, the BEP ratio must be optimized. If this ratio is too low, the material will not have enough group V material present. This generally results in high defect densities, and will often manifest as surface haziness. This can be easily diagnosed using a Nomarski microscope, where large defects will be present over the entire surface. On the other hand, if the ratio is too high, the results will manifest more in device characterization than in the

initial material characterizations. This typically is the result of smaller scale defects such as interstitial and antisite defects. In order to optimize the BEP ratio, several devices must be grown at different ratios to determine which results in the best device performance, which is the focus of this next study.

For the Ga-free SL, only the As:In BEP ratio can reasonably be optimized, since the Sb BEP ratio is set to provide the correct InAsSb composition, and thus cannot be altered independently. In order to optimize the As:In BEP ratio, a series of Ga-free SL PIN devices were grown. Each sample was grown at a different ratio, with the intent being that electrical characterizations would determine which ratio was preferable. Each of the samples had to be individually lattice matched, since varying the As:In BEP ratio will also vary the InAsSb composition, which must then be recalibrated by adjusting the Sb valve. The ratios selected initially were As:In ratios of 4:1, 5:1, 6:1, 7:1, and 9:1. Upon initial growth, however, the 4:1 BEP ratio came out hazy, which indicated that this ratio was too low to grow good Ga-free SL material. On the other side, the 9:1 ratio looked good at first glance, but the results from an XRD scan, shown in figure 5.1, showed several split peaks at each point where only one peak should exist. This indicates that the material quality had degraded, and the superlattice layer thicknesses and interfaces may not have been consistent throughout the epilayer. Due to this, full devices were grown only at 5:1, 6:1, and 7:1 As:In BEPs. XRD results for each of these growths can be seen in figure 5.1.

The samples themselves were all grown on top of GaSb:Te substrates. Oxide desorption was performed at 550°C for 30 minutes for each substrate. The buffer layer on each sample was a 300nm thick growth of GaSb doped n-type at $2{\cdot}10^{18}$ cm^{-3}. The devices were PIN structures based on the 14ML InAs - 12ML $InAs_{0.81}Sb_{0.19}$ superlattice. The bottom contact was grown 500nm thick and doped n-type at $2 \cdot 10^{18}$ cm^{-3}. The absorber layer for each device was grown 2μm thick and doped

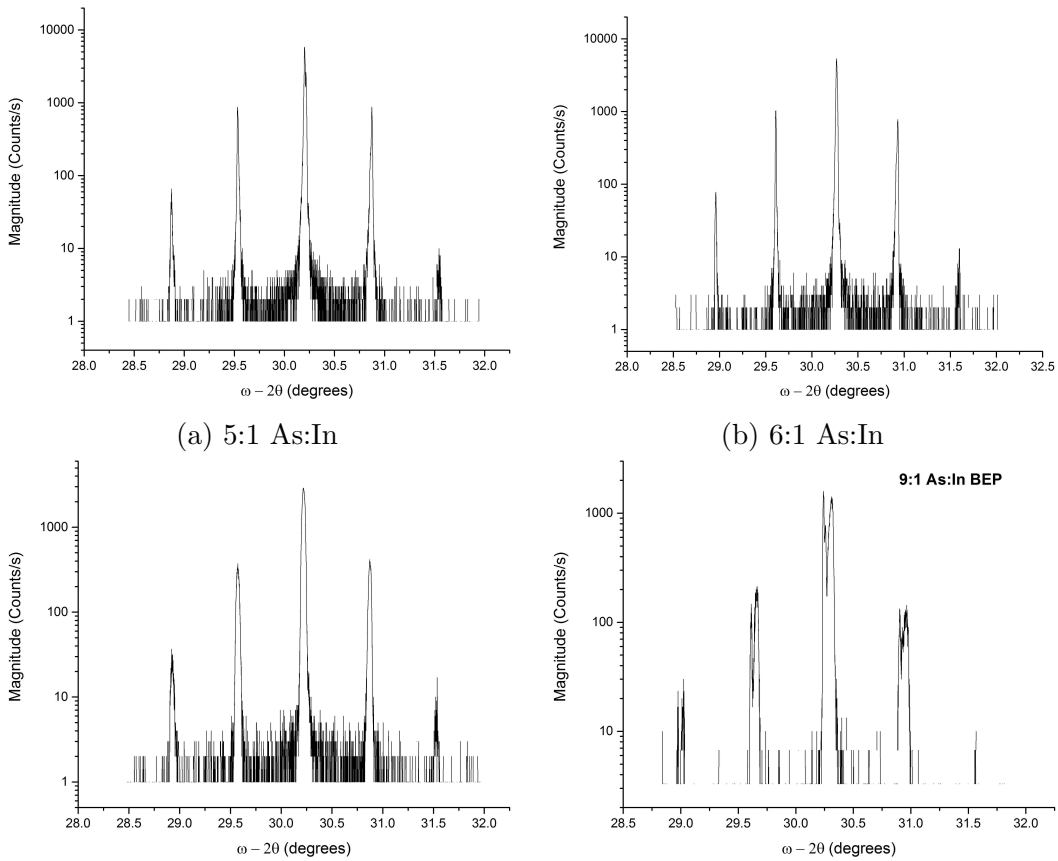

(a) 5:1 As:In

(b) 6:1 As:In

(c) 7:1 As:In

(d) 9:1 As:In

Figure 5.1: XRD rocking curves of each BEP ratio. 5:1, 6:1, and 7:1 all look like good SL samples, but 9:1 shows broad split peaks, indicating the quality of the material has degraded.

p-type at $3 \cdot 10^{16}$ cm^{-3}. The top contact was 200nm thick, and doped p-type $2 \cdot 10^{18}$ cm^{-3}. These structures were grown at 420°C, as measured by pyrometer.

Once the devices were complete, they were processed into square mesas of varying size. The mesa etch was a gas etch done in an ICP. The top and bottom contacts of the devices were metallized using the same Ti/Pt/Au recipe as used previously. The devices were passivated with SiN_x. The mesa sizes varied from 500μm down to 15μm squares. These processed devices were then taken for dark current and QE

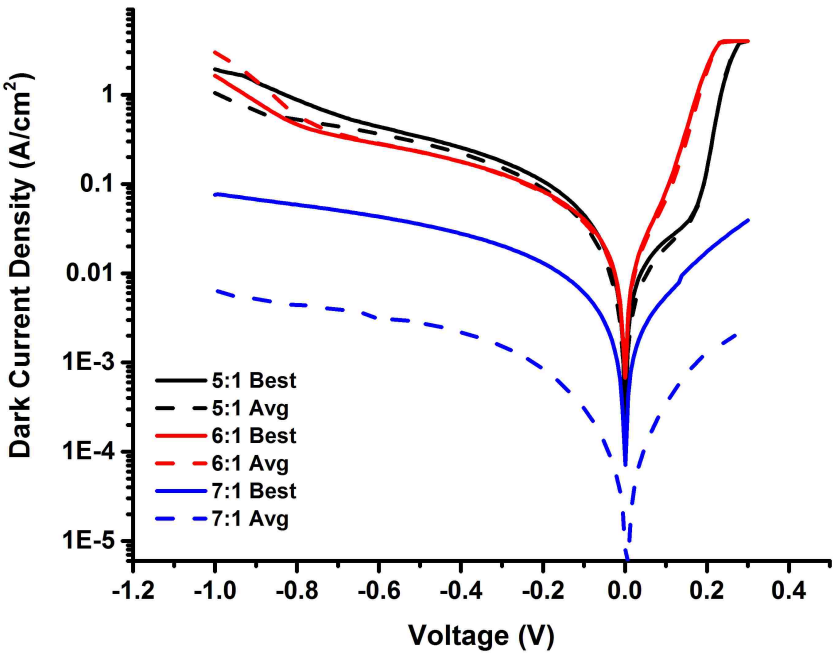

Figure 5.2: A comparison of both the best device and average results from the BEP study at 77K. The results indicate that the 7:1 As:In BEP shows a considerably lower dark current than the other BEP ratios. The best device for this ratio in particular showed good results.

characterizations.

The results from the dark current characterization are seen in figure 5.2. The 5:1 and 6:1 BEP ratio samples showed relatively similar performance. However, the 7:1 BEP ratio shows a clear reduction in dark current over the other samples. This particular sample overall shows an improvement even from previous studies, which is expected given the previous lack of BEP optimization.

The spectral response of these devices was measured to ensure that they match the designed cutoff wavelength. The results are shown in figure 5.3. The expected 5μm 0% cutoff is demonstrated by all samples.

The quantum efficiency for each sample was measured similarly to previous sam-

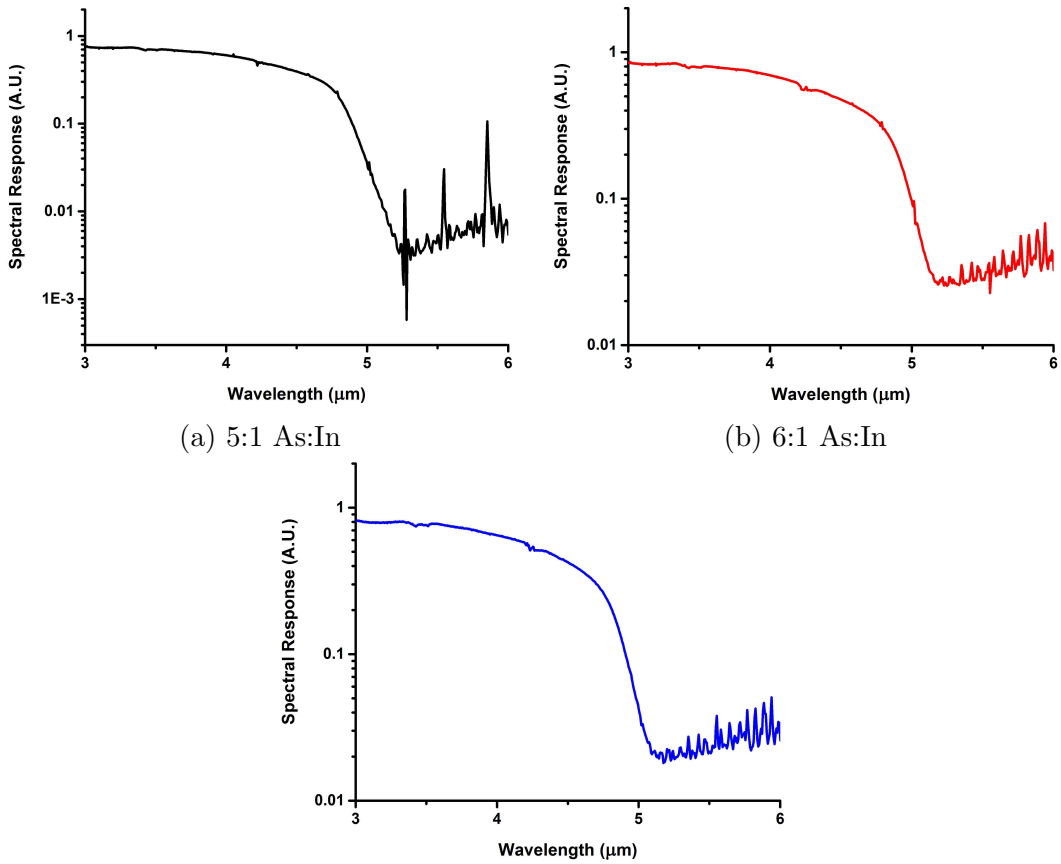

(a) 5:1 As:In

(b) 6:1 As:In

(c) 7:1 As:In

Figure 5.3: Spectral response results from the BEP study samples at 77K. These show that the samples match the designed 5μm 0% cutoff wavelength.

ples, and was calculated at a 0V bias. The results of this are shown in figure 5.1. The results indicate that the 7:1 BEP ratio produced the best device. This provides an initial round of optimization for the As:In BEP of Ga-free SL devices, but further work should be done to narrow down the BEP ratio further by using smaller increments centered around 7:1 As:In.

In conclusion, the effect of As:In BEP on the performance of Ga-free SL-based detector structures has been demonstrated. The BEP ratio shows a clear effect on both the dark current level and the quantum efficiency of grown detector structures.

As:In BEP	Best Device Dark IV -0.1V, 80K (A/cm^2)	Average Dark IV -0.1V, 80K (A/cm^2)	Quantum Efficiency (0V, 80K)
5:1	0.0400	0.04674	0.2915
6:1	0.0416	0.04149	0.3580
7:1	0.0003484	0.00626	0.4135

Table 5.1: A table of the results from the BEP study. These results indicate that an As:In BEP of 7:1 is preferable over lower BEP ratios.

The results from this study show the best performance at the highest tested BEP value of 7:1 As:In. Future studies may narrow down this ratio even further by testing BEP ratios around 7:1 in smaller increments (e.g. +/- 0.2).

Chapter 6

Modulated MBE Growth of the Ga-free SL

One major consideration in the growth of Ga-free SLs is the dependence of the InAsSb composition on both the source BEPs from the As and Sb cells and on the substrate temperature maintained during growth. This dependence is shown in section 2.5.6. In order to alleviate these problems, many groups use a technique called modulated MBE (MMBE), to reduce these dependencies [72]. The idea behind this is to replace the ternary material (InAsSb in this case) with two very thin binary materials (e.g. InAs and InSb). By using the correct proportions of binary layers, a specified composition of ternary material can be mimicked. This is accomplished through the use of rapid (1s) shuttering of the As and Sb sources. The figure in 2.5.6 shows the high degree of dependence on growth conditions exhibited by the superlattice. The effect of MMBE on the electrical performance of a Ga-free SL device had yet to be tested, however, and is the focus of this section.

The first step in this study was to design an MMBE-based structure that would properly mimic the ternary material used in Ga-free SL growth. The starting point

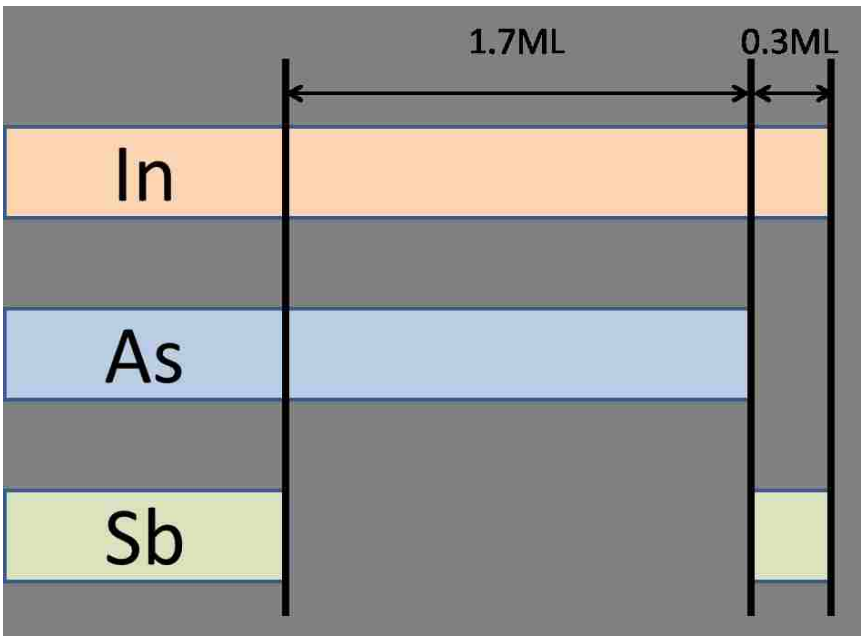

Figure 6.1: The shutter sequence used to grow the InAs-InSb layer meant to mimic an $InAs_{0.81}Sb_{0.19}$ ternary. The In shutter is kept open throughout, and the As and Sb shutters are sequenced to produce the desired results.[83]

for this was to use the 14ML InAs - 12ML $InAs_{0.81}Sb_{0.19}$ SL used in previous studies. The MMBE-grown InAs-InSb layer was then designed to replace the ternary material, using a layer thicknesses of 1.62ML InAs - 0.38ML InSb. This was done to maintain the same composition as the random-alloy ternary material. While these layer thicknesses will theoretically result in the same composition as the ternary material, in practice they did not. This composition resulted in a compressive strain on the superlattice, which indicated that the Sb composition was too high. In order to compensate for this, the composition of the InAs-InSb layer was adjusted to be 1.7ML InAs - 0.3ML InSb. This resulted in a superlattice that was lattice matched to the GaSb substrate, as is expected from the intended composition of the InAsSb ternary layer. The growth sequencing is depicted in figure 6.1.

Once the MMBE-based SL was calibrated, two PIN structure samples were grown

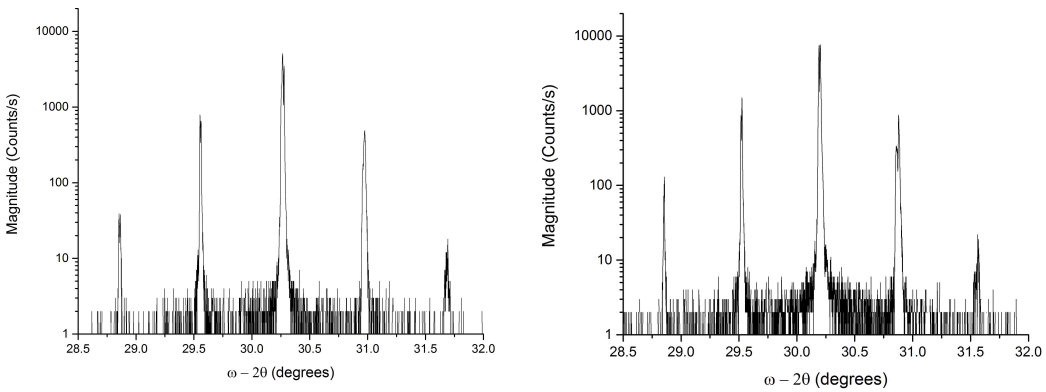

(a) Ternary reference sample (b) MMBE sample

Figure 6.2: XRD results from both the ternary and MMBE-based Ga-free SL samples. Both show good lattice match, though the MMBE-grown full-width at half-maximum of the 0^{th} order SL peak (28.8 arcsec) is thinner than that of the ternary (34.2 arcsec). Generally, thinner peaks indicate sharper interfaces between the superlattice layers.[83]

using a similar design to previous studies. One sample was a reference sample composed of 14ML InAs - 12ML $InAs_{0.81}Sb_{0.19}$ SL, while the other replaced the InAsSb layer with the calibrated InAs-InSb layer. This sample was grown in a VG V80H reactor, rather than the Gen10 used in other studies due to the heavy load on the Gen10 reactor at the time this study was performed. The buffer layer and contact layers for this sample were both doped at $2 \cdot 10^{18}$ cm^{-3}. The buffer itself was a 250nm thick GaSb layer grown at 500°C. The bottom contact was doped n-type and grown to be 500nm thick. The top contact was p-type, and was 80nm thick. The absorber layer was 2μm thick, and was doped p-type at $3 \cdot 10^{16}$ cm^{-3}. Once grown, the samples were analyzed using XRD to ensure that the epilayers remained lattice matched to the GaSb substrates as originally intended. The results of this are shown in figure 6.2.

These samples were processed using the same square mesa mask as used for the initial Ga-free SL device, shown in figure 3.4. The etch was performed in an ICP

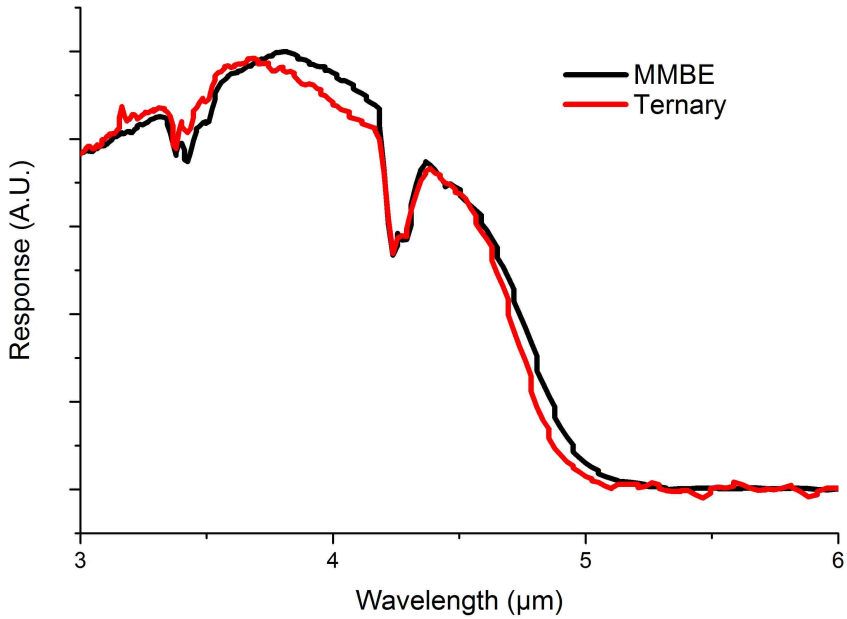

Figure 6.3: The comparison of the spectral response of the two PIN structure devices performed at 80K. This figure shows a roughly 5μm 0% cutoff wavelength, as expected from the design of the SL.[83].

machine using BCl_3 gas. The contacts and passivation were the same as in the initial device (Ti/Pt/Au contacts with SiN_x passivation). The resulting spectral response was tested to ensure a 5μm 0% cutoff wavelength at 80K. The comparison of the results for the two samples can be seen in figure 6.3. The full temperature dependent spectral response data can be seen in figure 6.4.

As in previous studies, the devices were characterized for both quantum efficiency and dark current characteristics. A comparison of the dark current results from the MMBE and ternary samples at 80K can be seen in figure 6.5. These results indicate that the MMBE-based sample produced slightly better results than the ternary material, which is in line with the other characterizations performed so far.

The final piece of data comes from the quantum efficiency of both devices. These measurements were performed at CHTM using the same setup as previous studies,

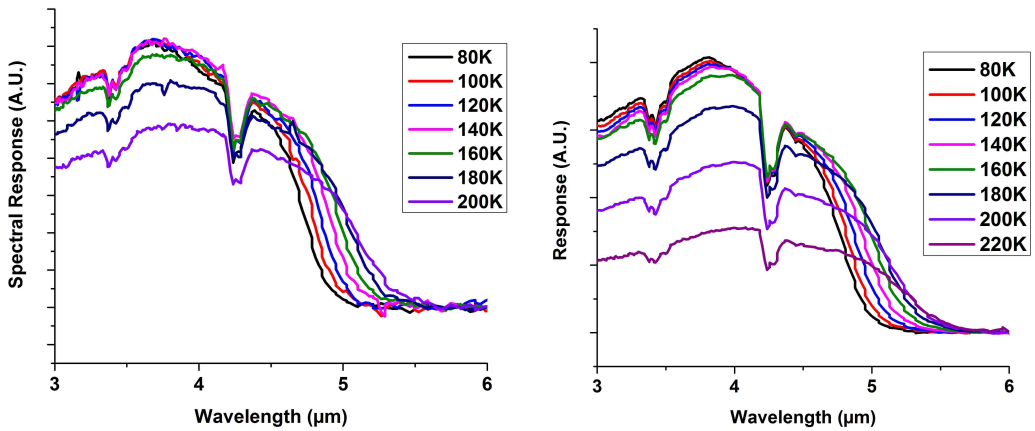

(a) Ternary reference sample (b) MMBE sample

Figure 6.4: The temperature dependent spectral response results for both the ternary and MMBE-based Ga-free SL devices.[83]

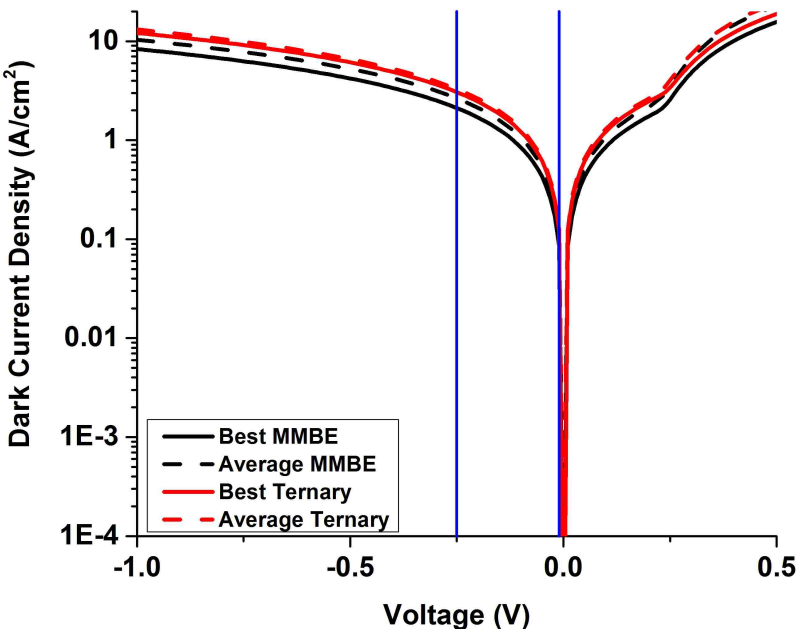

Figure 6.5: A comparison of the dark current demonstrated by the MMBE-based and ternary-based Ga-free SL devices at 80K. Both the best device and average dark currents are shown, with blue lines indicating $V_b = -0.01V$ and $V_b = -0.25V$. At -0.25V, the dark current levels are 4.249 A/cm^2 for the ternary and 3.522 A/cm^2 for the MMBE sample.[83]

with the Mikron blackbody source set at 627°C. A plot of QE vs. bias voltage can be seen in figure 6.6. The MMBE device, at a QE of roughly 40%, indicates a clear improvement in performance when compared to the ternary sample, showing a QE of roughly 24%, here. A full comparison of the performance of the two samples can be seen in figure 6.1. The ternary itself has QE comparable to that of the initial device. From the other studies in this dissertation, the highest QE obtained from the ternary-based Ga-free SL devices is comparable to that obtained by the MMBE-based device here, which indicates that MMBE will work as a replacement for the ternary layer in Ga-free SL devices.

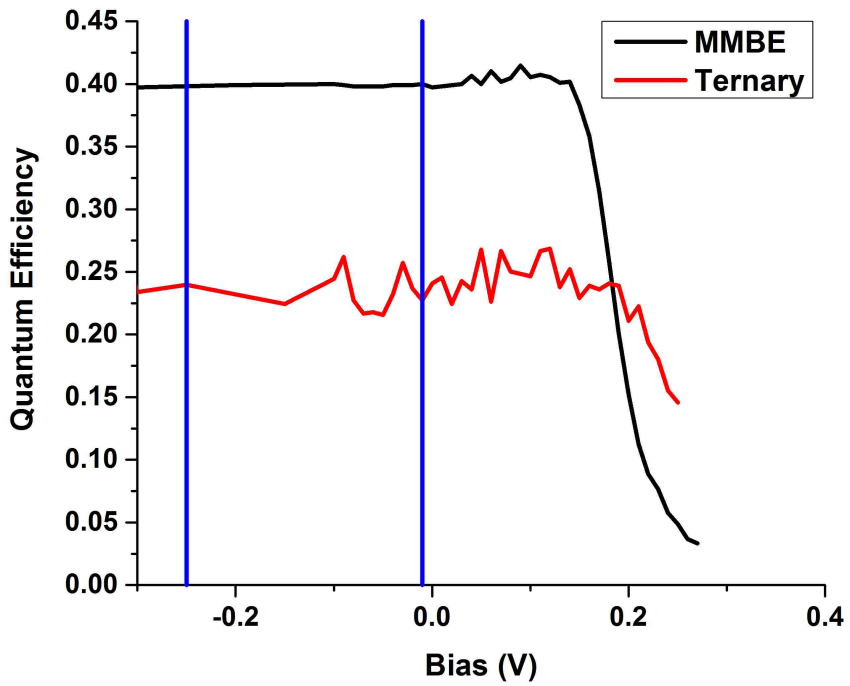

Figure 6.6: The QE demonstrated by both the best MMBE-based and ternary-based devices. This shows that the MMBE QE is clearly higher than the ternary. As with the dark current measurements, the blue lines indicate $V_b = -0.01V$ and $V_b = -0.25V$.[83]

Sample	Average Dark Current (A/cm^2)	Best Device Dark Current (A/cm^2)	Quantum Efficiency
MMBE (-0.01V, 80K)	0.1068	0.0853	39.7
Ternary (-0.01V, 80K)	0.1315	0.1227	24.1
MMBE (-0.25V, 80K)	3.522	2.115	39.9
Ternary (-0.25V, 80K)	4.249	2.859	24.0

Table 6.1: This table summarizes the results of the measurements done on both the MMBE-based and ternary-based Ga-free SL devices. The results indicate that MMBE can be used in place of the ternary for future devices.[83]

Chapter 7

InAs-on-InAsSb Interface

The purpose of the final study performed for this dissertation is to determine if the introduction of an interface layer can improve the quality of a Ga-free SL device. This was spurred by the fact that the InAs-GaSb superlattice contains interface layers at both the InAs-on-GaSb and GaSb-on-InAs interfaces. Furthermore, it has been indicated in literature that the InAs-on-InAsSb interface in the Ga-free SL has a larger degree of intermixing at the interface than the InAsSb-on-InAs surface [44, 84]. This indicates that the optimization of the InAsSb-on-InAs will have a lesser effect on the resulting device performance. Due to this, the study described in this chapter focuses on optimizing the InAs-on-InAsSb interface layer. Both this study and the referenced study in literature use the MMBE technique to grow the InAsSb material.

In order to improve this interface, this study introduces a variety of layers at the interface to attempt to prevent any Sb left on the surface from migrating into the following InAs layer. This is done through several methods, including a short growth interrupt, an As soak, an AlSb layer, and finally a short Al soak. These will be compared to an SL reference sample that has no special interface layers. The shutter sequencing for these growths is depicted in figure 7.1. These sequences use

the previously-characterized superlattice design of 14ML InAs - 12ML InAsSb, and assume a growth rate of 0.3ML/sec.

This series of samples was grown using InAs-InSb MMBE in place of the InAsSb material. These samples were grown in a VG V80H MBE machine on 2" GaSb:Te substrates. Oxide desorption was performed at 550°C for 20 minutes. Following that, a 300nm thick GaSb:Te buffer was grown to smooth the surface prior to device growth. All samples were grown at a growth temperature estimated to be 420°C using the transition temperature that can be seen through RHEED analysis of GaSb. The devices were grown as PIN structure devices with the same design as in previous studies. HRXRD results from the grown wafers can be seen in figure 7.2. The results show that the superlattices are all a slight amount compressive (roughly 100 arcseconds for each sample). However, the AlSb is considerably more compressive than the other samples, which is expected due to the fact that AlSb is compressive on GaSb.

The grown structures were processed into mesas using a similar procedure as described in the BEP study. The etch resulted in square mesas of varied sizes, ranging from 15μm up to 500μm per side. Top and bottom contacts were composed of the same Ti/Pt/Au recipe used previously, and once again SiN_x passivation was used. The dark current and quantum efficiency of the devices were then measured.

The dark current results from the interface study are shown in figure 7.3. The best device results indicate that the reference sample is better than any of the special interface layers. However, the average results indicate that the AlSb layer and As soak devices are both better than the reference. These results do not provide a definitive conclusion as to which device is overall best. The initial determination at this point is only that the dark currents of the Al flash and growth interrupt are higher than the other three devices, and thus are not likely the best methods for optimizing the interface layer. The next step is to analyze quantum efficiency to see

if any conclusion can be drawn from that data.

The spectral response of each device, shown in figure 7.4, indicates that the samples all roughly fall into the designed 5μm 0% cutoff wavelength that the superlattice is designed to provide. The Al flash and AlSb samples show a shift in the cutoff from the other devices, indicating that the presence of an Al-based layer has an influence on the overall superlattice bandgap. The Al flash sample shows a blueshift, which is likely due to the formation of a random composition AlInAsSb layer. By contrast, the AlSb layer shows a redshift, which may either be due to the layer itself or to diffusion and incorporation of excess Sb in the superlattice layers.

The quantum efficiency was the last measured parameter from these devices. The results are listed in the table in figure 7.1. The As soak interface layer demonstrated the highest quantum efficiency, though it was not much above the reference sample. All other interface layers showed a reduced QE compared to the reference, indicating that these layers do not improve the performance of the Ga-free superlattice. The quantum efficiencies varied from 42.65% at the low end (from the Al flash device) up to 52.13% at the high end (from the As soak device).

The data from this study indicates that the introduction of a growth interrupt, an Al flash, or an AlSb layer at the InAs-on-InAsSb interface does not improve the performance of a Ga-free superlattice-based device. However, the introduction of an As soak at this interface may show improvement upon further optimization of the duration of this soak. The initial results show a slight improvement in quantum efficiency. The average dark current level demonstrated by the As soak device was lower than that of the reference sample, though the best device dark current was higher than the reference. The difference between the average and best device dark current levels on the As soak device is much lower than that of the reference, which indicates that the overall uniformity of the resulting devices is improved. The introduction of an As soak at the InAs-on-InAsSb interface is thus worthy of further study.

Interface Layer	Best Device Dark IV -0.1V, 80K (A/cm^2)	Average Dark IV -0.1V, 80K (A/cm^2)	Quantum Efficiency (0V, 80K)
Interrupt	0.02920	0.03256	0.4936
AlSb	0.00340	0.01081	0.4929
Al Flash	0.02720	0.36335	0.4265
As Soak	0.00314	0.00923	0.5213
Reference	0.00132	0.02338	0.5194

Table 7.1: This table shows the results for each different interface layer used. From the best device and average dark current results, it is difficult to determine which interface layer is preferable. However, it can be noted that the interrupt and Al flash layers did not perform as well as the other three. The quantum efficiency results indicate that an As soak may demonstrate a slight improvement.

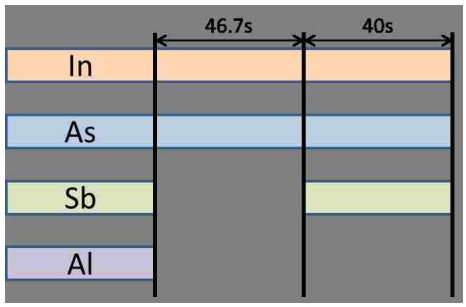

(a) Reference SL sample

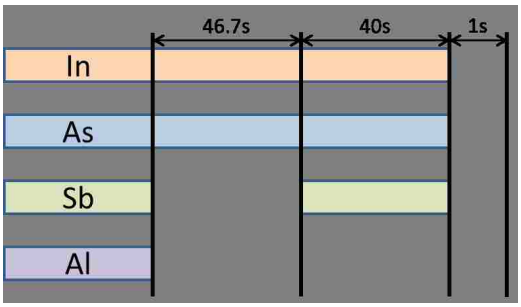

(b) SL sample with growth interrupt.

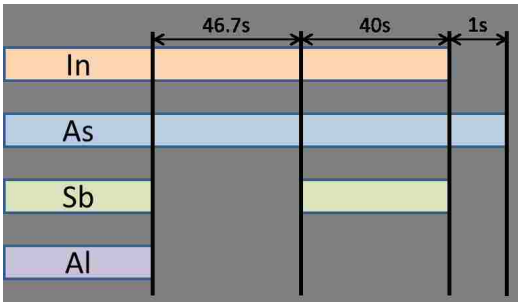

(c) SL sample with As soak.

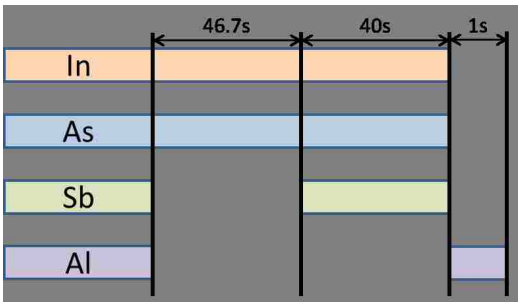

(d) SL sample with Al flash.

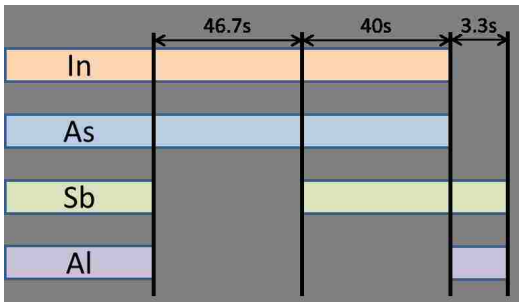

(e) SL sample with AlSb layer

Figure 7.1: The shutter displaying the interface layers used in this study. The sequence repeats at the end of each diagram. These diagrams are created assuming a growth rate of 0.3ML/sec and a 14ML InAs - 12ML InAsSb superlattice.

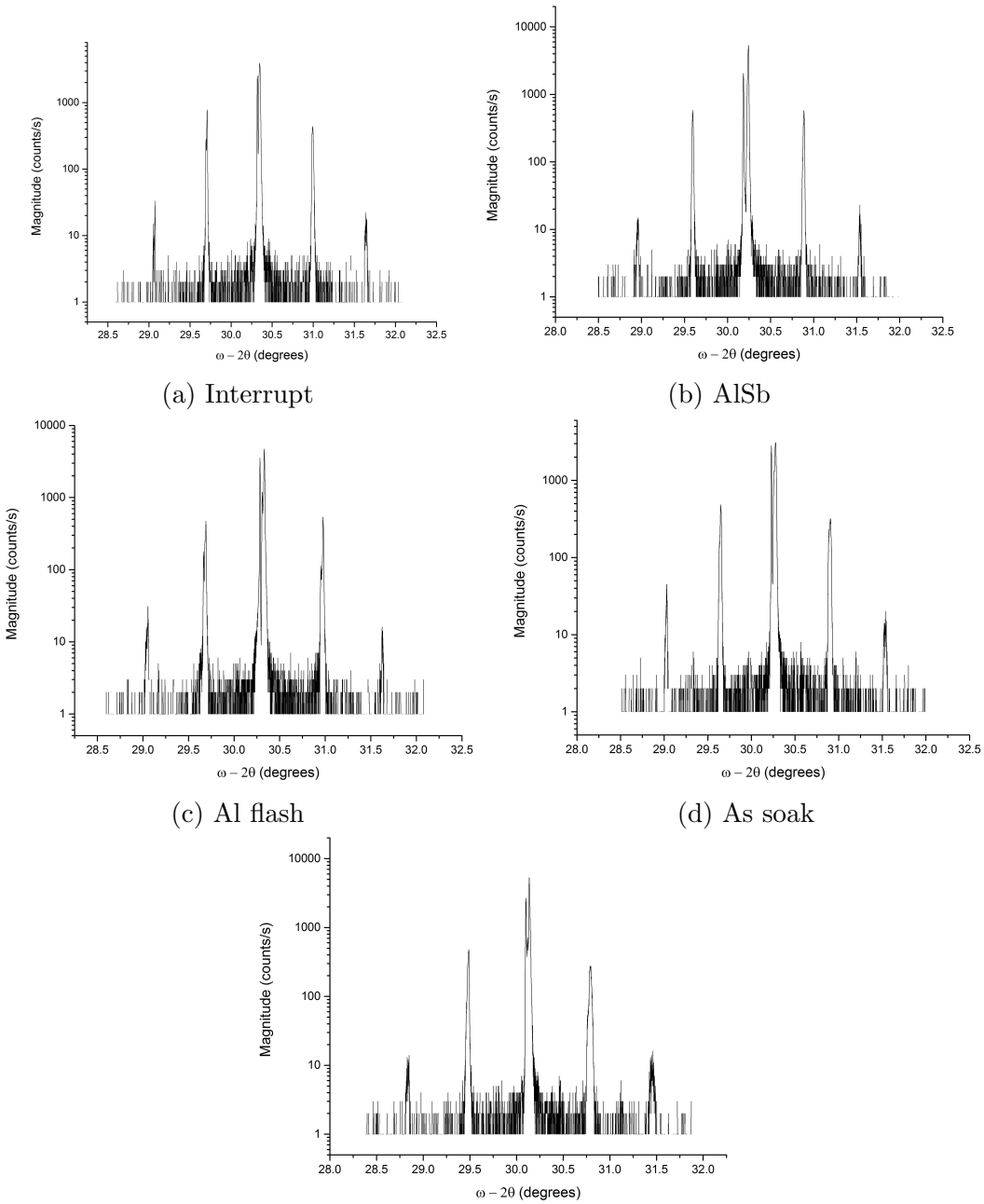

(a) Interrupt

(b) AlSb

(c) Al flash

(d) As soak

(e) Reference

Figure 7.2: HRXRD results from the samples grown for the interface study. These results show the samples to have a slight amount of compressive strain. The AlSb is considerably more compressive than the other samples, which is expected since AlSb is compressive on GaSb.

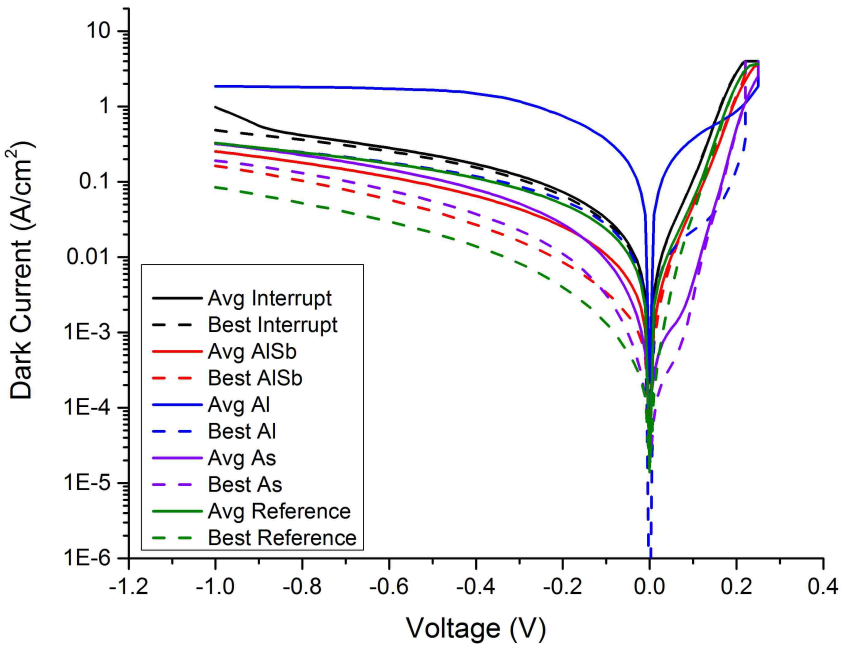

Figure 7.3: Dark current comparison between each device at 80K. Both the best device and average results (averaged over 6 or more devices per interface layer) are reported. These results are not conclusive as to which technique is preferable.

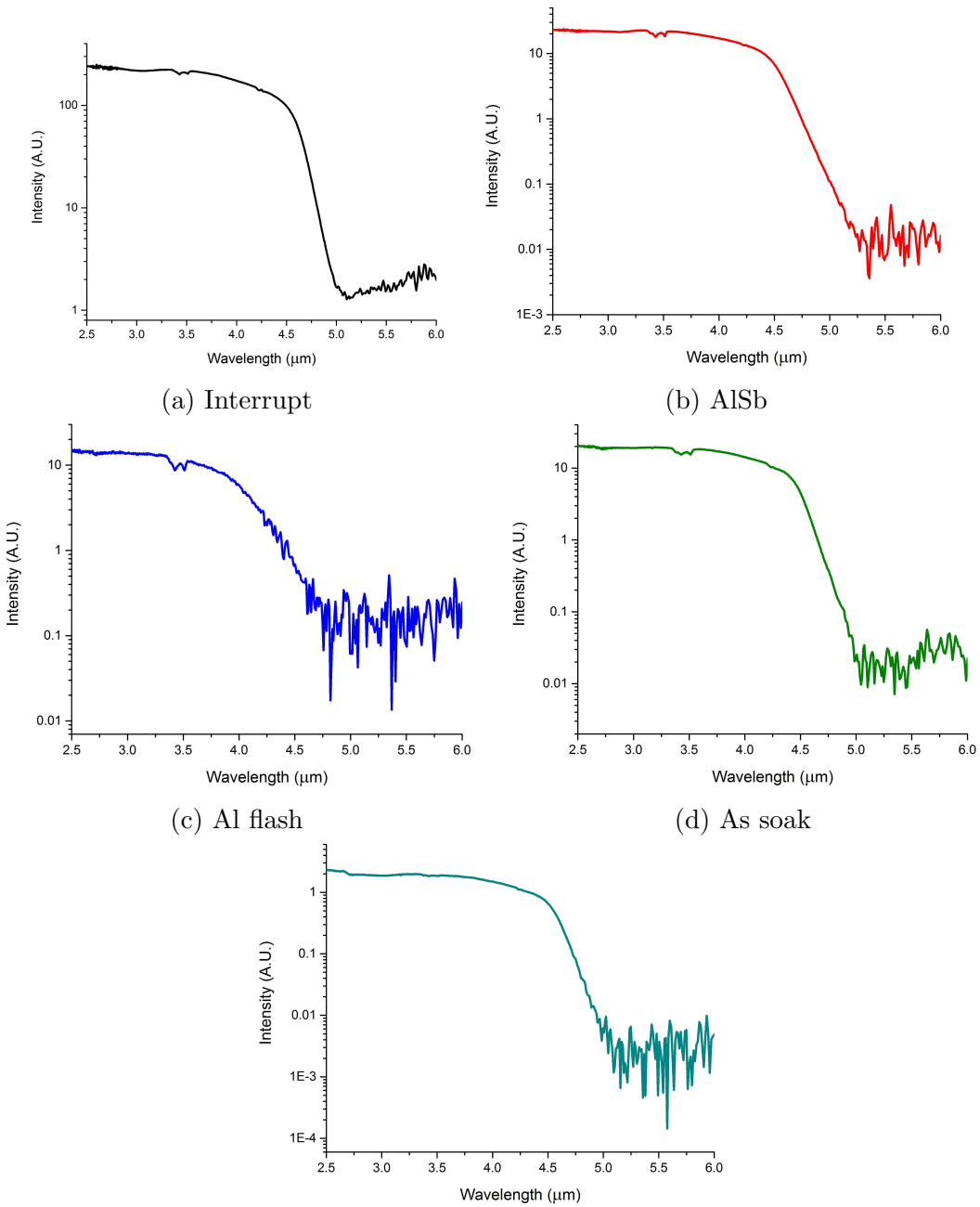

(a) Interrupt

(b) AlSb

(c) Al flash

(d) As soak

(e) Reference

Figure 7.4: Spectral response results from each sample at 80K. The 0% cutoff wavelength for most is roughly 5μm, which matches the design of the superlattice. Both aluminum containing devices show slightly shifted cutoff wavelengths from the other devices. For the Al flash, this is likely due to the formation of a random composition AlInAsSb layer at the interface.

Chapter 8

Conclusion

The Ga-free strained-layer superlattice material has the potential to greatly improve the performance of high-end infrared detectors and imaging systems. This has spurred recent interest in the research and development of this material. The high carrier lifetime in Ga-free superlattice combined with the natural suppression of Auger recombination present in superlattice materials shows great promise which has not yet been fully realized.

All devices grown in this dissertation were PIN-structure MWIR detectors made from a Ga-free SL. The first electrical characterization of a Ga-free SL device was presented initially, along with some initial modeling for the resulting dark current. This experiment showed that the dark current was considerably higher than expected, given the SRH lifetimes demonstrated by the Ga-free SL in literature.

The next experiment tested the results of some light p-type doping in the absorber region of the detectors. InAs-InAsSb materials are innately n-type, so a light p-type doping was introduced in order to encourage more intrinsic-like behavior. The results from this study showed that a doping level of $3 \cdot 10^{16}$ cm^{-3} exhibited better results than lower doping levels. This was determined via dark current and quantum

efficiency characterization of a series of devices with varied absorber doping levels.

The third experiment reported in this dissertation examined the As:In BEP ratio used during the growth of Ga-free SL devices. This ratio is known to be an important parameter in the growth of other materials, and thus needed to be optimized in order to improve the quality of the Ga-free SL material used in MBE-grown detectors. As in the doping level study, this experiment examined the resultant dark current and quantum efficiencies from a series of detectors grown at varied As:In BEP ratios. This study showed that a ratio of As:In at 7:1 produced better results than lower BEP ratios. This is attributed to a reduction in the number of defects present in the grown Ga-free SL material.

The next study focused on improving the repeatability and reliability of Ga-free SL growth by looking into the use of a modulated MBE (MMBE)-based InAs-InSb material in place of the InAsSb ternary material. This is done because the MMBE-based material (or MMBE technique) is far less dependent on the growth temperature and source BEP values remaining extremely stable throughout the growth. Unlike previous studies, this one focused on the performance of a device grown using this technique. The device grown using the MMBE technique showed improved performance, via dark current and quantum efficiency characterizations, thereby indicating that it may be used successfully in detector devices.

The final study examined the InAs-on-InAsSb interface. The purpose here was to reduce the probability that some of the Sb left at the interface after the growth of the InAsSb layer, grown via the MMBE technique, would diffuse into the subsequent InAs layer. This study tested the addition of several different layers added between the InAsSb and InAs layer in order to discourage this diffusion. These layers included a brief growth interrupt, an As soak, an Al flash, and a thin AlSb layer. The results from this study were not as straightforwardly conclusive as in previous studies. The dark current and quantum efficiency indicate that the As soak and AlSb layers both

Study	Description	Devices Tested	Best Result Based on Electrical Characterization
Absorber Doping	Varied p-type doping in absorber region of MWIR PIN devices.	NID, $5 \cdot 10^{15}$, $1 \cdot 10^{16}$, $3 \cdot 10^{16}$	$3 \cdot 10^{16}$
As:In BEP Ratio	Varied As:In BEP ratio in MWIR PIN devices	5:1, 6:1, 7:1	7:1
Digital Alloy	InAs-InSb digital alloy used in place of InAsSb ternary	Digital Alloy, Ternary	Digital Alloy comparable/better
InAs-on-InAsSb Interface	Various growth layers introduced at InAs-on-InAsSb interface	Reference, Interrupt, Al flash, AlSb, As soak	Results close, As soak most promising

Table 8.1: Summary of results from various studies performed for this dissertation

showed roughly comparable performance to the reference sample. Given these results, it would be wise to further examine the As soak in particular as a potential method for improving this interface.

In conclusion, this dissertation provides data from a series of experiments aimed at improving the performance of Ga-free superlattice devices. The primary focus has been in the design and growth of the superlattice material itself, rather than either the design of barrier structures or the processing of the Ga-free SL material. The results here are intended to be used to assist future researchers in the growth of Ga-free SL-based devices. A summary of the results from these studies is provided in figure 8.1.

Chapter 9

Future Work

This thesis provided some initial studies on optimizing the growth of InAs-InAsSb SL-based devices. The natural progression for this work is to take the initial results and further narrow down the growth conditions through similar studies. The improvements suggested are listed below.

- Absorber doping
    1. Continue raising the doping level beyond $3 \cdot 10^{16}$ p-type to look for further improvement
    2. Check the effects of doping only a single SL layer rather than both
- Ga-free growth BEP
    1. Further narrow down the optimal BEP ratio (e.g. 7.2:1 vs. 6.8:1 As:In)
- Interface study
    1. Varied layer times and/or thicknesses can be tested to further examine the results

2. Optimization of an As soak layer

- Processing

1. The processing of Ga-free superlattice devices has not been covered in this dissertation. Optimization of the device fabrication, particularly the material used in device passivation, is ripe for study.

References

[1] B. Klein, *Defect Investigations in InAs/GaSb Type-II Strained Layer Superlattice*. PhD thesis, University of New Mexico, 2014.

[2] D. L. Smith and C. Mailhiot, "Proposal for strained type II superlattice infrared detectors," *Journal of Applied Physics*, vol. 62, no. 6, 1987.

[3] C. H. Grein, H. Cruz, M. E. Flatté, and H. Ehrenreich, "Theoretical performance of very long wavelength InAs/InxGa1 xSb superlattice based infrared detectors," *Applied Physics Letters*, vol. 65, no. 20, pp. 2530–2532, 1994.

[4] E. R. Youngdale, J. R. Meyer, C. A. Hoffman, F. J. Bartoli, C. H. Grein, P. M. Young, H. Ehrenreich, R. H. Miles, and D. H. Chow, "Auger lifetime enhancement in InAs-$Ga_{1-x}In_xSb$ superlattices," *Applied Physics Letters*, vol. 64, 1994.

[5] W. Tennant, D. Lee, M. Zandian, E. Piquette, and M. Carmody, "MBE HgCdTe Technology: A Very General Solution to IR Detection, Described by Rule 07, a Very Convenient Heuristic," *Journal of Electronic Materials*, vol. 37, no. 9, pp. 1406–1410, 2008.

[6] E. H. Steenbergen, B. C. Connelly, G. D. Metcalfe, H. Shen, M. Wraback, D. Lubyshev, Y. Qiu, J. M. Fastenau, A. W. K. Liu, S. Elhamri, O. O. Cellek, and Y.-H. Zhang, "Significantly improved minority carrier lifetime observed in a long-wavelength infrared III-V type-II superlattice comprised of InAs/InAsSb," *Applied Physics Letters*, vol. 99, 2011.

[7] B. V. Olson, E. A. Shaner, J. K. Kim, J. F. Klem, S. D. Hawkins, L. M. Murray, J. P. Prineas, M. E. Flatté, and T. F. Boggess, "Time-resolved optical measurements of minority carrier recombination in a mid-wave infrared InAsSb alloy and InAs/InAsSb superlattice," *Applied Physics Letters*, vol. 101, 2012.

[8] A. M. Hoang, G. Chen, R. Chevallier, A. Haddadi, and M. Razeghi, "High performance photodiodes based on InAs/$InAs_{1-x}Sb_x$ type-II superlattices for very long wavelength infrared detection," *Applied Physics Letters*, vol. 104, 2014.

[9] A. Haddadi, S. R. Darvish, G. Chen, A. M. Hoang, B. M. Nguyen, and M. Razeghi, "High operability 1024 x 1024 long wavelength type-ii superlattice focal plane array," *J. Quant. Electron.*, vol. 48, 2012.

[10] E. A. Plis, *Mid-IR Type-II InAs/GaSb Nanoscale Superlattice Sensors*. PhD thesis, University of New Mexico, 2007.

[11] J. Shao, *Engineered Quantum Dots for Infrared Photodetectors*. PhD thesis, University of New Mexico, 2011.

[12] A. Khoshakhlagh, *Longwave and Bi-color Type-II InAs/(In)GaSb Superlattice Infrared Detectors*. PhD thesis, University of New Mexico, 2010.

[13] M. A. Kinch, *Fundamentals of Infrared Detectors*. SPIE Press, 2007.

[14] Q. K. Yang, F. Fuchs, J. Schmitz, and W. Pletschen, "Investigation of trap-assisted tunneling current in InAs/(GaIn)Sb superlattice long-wavelength photodiodes," *Applied Physics Letters*, vol. 81, 2002.

[15] P. Chakrabarti, A. Gawarikar, V. Mehta, and D. Garg, "Effect of Trap-assisted Tunneling (TAT) on the Performance of Homojunction Mid-Infrared Photodetectors based on InAsSb," *Journal of Microwaves and Optoelectronics*, vol. 5, no. 1, 2006.

[16] P. Martyniuk, J. Wróbel, E. Plis, P. Madejczyk, A. Kowalewski, W. Gawron, S. Krishna, and A. Rogalski, "Performance modeling of MWIR InAs/GaSb/B-$Al_{0.2}Ga_{0.8}Sb$ type-II superlattice nBn detector," *Semicond. Sci. Technol.*, vol. 27, 2012.

[17] P. Martyniuk, J. Wróbel, E. Plis, P. Madejczyk, W. Gawron, A. Kowalewski, S. Krishna, and A. Rogalski, "Modeling of midwavelength infrared InAs/GaSb type II superlattice detectors," *Optical Engineering*, vol. 52, p. 061307, jan 2013.

[18] C. H. Grein, P. M. Young, and H. Ehrenreich, "Minority carrier lifetimes in ideal InGaSb/InAs superlattices," *Applied Physics Letters*, vol. 61, 1992.

[19] L. Esaki and R. Tsu, "Superlattice and negative conductivity in semiconductors," tech. rep., IBM Res. Note, RC-2418, March 1969.

[20] L. Esaki and R. Tsu, "Superlattice and Negative Differential Conductivity in Semiconductors," *IBM Journal of Research and Development*, vol. 14, 1970.

[21] G. A. Sai-Halasz, R. Tsu, and L. Esaki, "A new semiconductor superlattice," *Applied Physics Letters*, vol. 30, 1977.

[22] H. J. Haugan, F. Szmulowicz, G. J. Brown, and K. Mahalingam, "Optimization of mid-infrared InAs/GaSb type-II superlattices," *Applied Physics Letters*, vol. 84, no. 26, pp. 5410–5412, 2004.

[23] M. R. Kitchin and M. Jaros, "Characterization of GaSb/InAs type II infrared detectors at very long wavelengths: Carrier scattering at defect clusters," *Physica E: Low-Dimensional Systems and Nanostructures*, vol. 18, no. 4, pp. 498–508, 2003.

[24] C. H. Grein, J. Garland, and M. Flatté, "Strained and Unstrained Layer Superlattices for Infrared Detection," *Journal of Electronic Materials*, vol. 38, no. 8, 2009.

[25] D. H. Chow, R. H. Miles, J. N. Schulman, D. A. Collins, and T. C. McGill, "Type II superlattices for infrared detectors and devices," *Semiconductor Science and Technology*, vol. 6, pp. C47–C51, 1999.

[26] H. J. Haugan, G. J. Brown, and L. Grazulis, "Effect of interfacial formation on the properties of very long wavelength infrared inas/gasb superlattices," *JVST B: Microelectronics and Nanomaterials*, vol. 29, no. 3, 2010.

[27] Y. Wei, W. Ma, Y. Zhang, J. Huang, Y. Cao, and K. Cui, "High structural quality of type ii inas/gasb superlattices for very long wavelength infrared detection by interface control," *J. Quant. Electron.*, vol. 48, 2012.

[28] R. Rehm, M. Walther, J. Schmitz, F. Rutz, J. Fleißner, R. Scheibner, and J. Ziegler, "InAs/GaSb superlattices for advanced infrared focal plane arrays," *Infrared Physics and Technology*, vol. 52, no. 6, pp. 344–347, 2009.

[29] G. Bishop, E. Plis, J. B. Rodriguez, Y. D. Sharma, H. S. Kim, L. R. Dawson, and S. Krishna, "nBn detectors based on InAsGaSb type-II strain layer superlattice," *Journal of Vacuum Science & Technology B: Microelectronics and Nanometer Structures*, vol. 26, no. 3, pp. 1145–1148, 2008.

[30] D. Z. Y. Ting, C. J. Hill, A. Soibel, S. A. Keo, J. M. Mumolo, J. Nguyen, and S. D. Gunapala, "A high-performance long wavelength superlattice complementary barrier infrared detector," *Applied Physics Letters*, vol. 95, no. 2, 2009.

[31] I. Vurgaftman, E. H. Aifer, C. L. Canedy, J. G. Tischler, J. R. Meyer, J. H. Warner, E. M. Jackson, G. Hildebrandt, and G. J. Sullivan, "Graded band

gap for dark-current suppression in long-wave infrared W-structured type-II superlattice photodetectors," *Applied Physics Letters*, vol. 89, no. 121114, 2006.

[32] J. B. Rodriguez, E. Plis, G. Bishop, Y. D. Sharma, H. Kim, L. R. Dawson, and S. Krishna, "nBn structure based on InAs/GaSb type-II strained layer superlattices," *Applied Physics Letters*, vol. 91, no. 043514, 2007.

[33] H. S. Kim, E. Plis, J. B. Rodriguez, G. D. Bishop, Y. D. Sharma, L. R. Dawson, S. Krishna, J. Bundas, R. Cook, D. Burrows, R. Dennis, K. Patnaude, A. Reisinger, and M. Sundaram, "Mid-IR focal plane array based on type-II InAs/GaSb strain layer superlattice detector with nBn design," *Applied Physics Letters*, vol. 92, no. 183502, 2008.

[34] N. Gautam, H. S. Kim, M. N. Kutty, E. Plis, L. R. Dawson, and S. Krishna, "Performance improvement of longwave infrared photodetector based on type-II InAs/GaSb superlattices using unipolar current blocking layers," *Applied Physics Letters*, vol. 96, no. 231107, 2008.

[35] N. Gautam, *Unipolar Barrier Strained Layer Superlattice Infrared Photodiodes: Physics and Barrier Engineering*. PhD thesis, University of New Mexico, 2012.

[36] Z. Tian, R. T. Hinkey, R. Q. Yang, D. Lubyshev, Y. Qiu, J. M. Fastenau, W. K. Liu, and M. B. Johnson, "Interband cascade infrared photodetectors with enhanced electron barriers and p-type superlattice absorbers," *Applied Physics Letters*, vol. 111, 2012.

[37] D. R. Rhiger, "Performance Comparison of Long-Wavelength Infrared Type II Superlattice Devices with HgCdTe," *Journal of Electronic Materials*, vol. 40, no. 8, 2011.

[38] D. Donetsky, S. P. Svensson, L. E. Vorobjev, and G. Belenky, "Carrier lifetime measurements in short-period InAs/GaSb strained-layer superlattice structures," *Applied Physics Letters*, vol. 95, 2009.

[39] S. P. Svensson, D. Donetsky, D. Wang, H. Hier, F. J. Crowne, and G. Belenky, "Growth of type II strained layer superlattice, bulk InAs and GaSb materials for minority lifetime characterization," *Journal of Crystal Growth*, vol. 334, pp. 103–107, 2011.

[40] W. Shockley and W. T. Read, "Statistics of the Recombination of Holes and Electrons," *Physical Review*, vol. 87, no. 5, pp. 835–842, 1952.

[41] W. Walukiewicz, "Defect reactions at metal-semiconductor and semiconductor-semiconductor interfaces," in *Symposium D Chemistry and Defects in Semiconductor Heterostructures*, vol. 148 of *MRS Proceedings*, 1989.

[42] Y.-H. Zhang, "Continuous wave operation of $InAs/InAs_xSb_{1-x}$," *Applied Physics Letters*, vol. 66, 1995.

[43] Y.-H. Zhang, R. H. Miles, and D. H. Chow, "Infrared Lasers Grown on InAs Substrates," *IEEE Journal of Selected Topics in Quantum Electronics*, vol. 1, no. 2, pp. 749–756, 1995.

[44] A. Y. Lew, E. T. Yu, and Y.-H. Zhang, "Atomic-scale structure of $InAs/InAs_xSb_{1-x}$ superlattices grown by modulated molecular beam epitaxy," *Applied Physics Letters*, vol. 14, 1996.

[45] Y.-H. Zhang, "InAs/$InAs_xSb_{1-x}$ type-II superlattice midwave infrared lasers," in *Optoelectronic Properties of Semiconductors and Superlattices: Antimonide-Related Strained-Layer Heterostructures* (M. O. Manasreh, ed.), vol. 3, pp. 461–500, 1997.

[46] E. H. Steenbergen, O. O. Cellek, D. Lubyshev, Y. Qiu, J. M. Fastenau, A. W. K. Liu, and Y.-H. Zhang, "Study of the valence band offsets between InAs and $InAs_{1-x}Sb_x$ alloys," *Proceedings of SPIE: Quantum Sensing and Nanophotonic Devices IX*, vol. 8268, 2012.

[47] D. Lackner, O. J. Pitts, M. Steger, A. Yang, M. L. W. Thewalt, and S. P. Watkins, "Strain balanced InAs/InAsSb superlattice structures with optical emission to 10 μm," *Applied Physics Letters*, vol. 95, 2009.

[48] E. H. Steenbergen, B. C. Connelly, G. D. Metcalfe, H. Shen, M. Wraback, D. Lubyshev, Y. Qiu, J. M. Fastenau, A. W. K. Liu, S. Elhamri, O. O. Cellek, and Y.-H. Zhang, "Temperature-dependent minority carrier lifetimes of $InAs/InAs_{1-x}Sb_x$ type-II superlattices," *Proceedings of SPIE: Infrared Sensors, Devices, and Applications II*, vol. 8512, 2012.

[49] A. Haddadi, G. Chen, R. Chevallier, A. M. Hoang, and M. Razeghi, "InAs/$InAs_{1-x}Sb_x$ type-II superlattices for high performance long wavelength infrared detection," *Applied Physics Letters*, vol. 105, 2014.

[50] Z.-Y. Lin, J. Fan, S. Liu, and Y.-H. Zhang, "Photoluminescence study of carrier recombination processes in InAs/InAsSb type-II superlattices," *Proceedings of SPIE: Infrared Technology and Applications XLI*, vol. 9451, 2015.

[51] C. H. Grein, M. E. Flatté, and H. Ehrenreich, "Comparison of Ideal InAs/InAs(1-x)Sb(x) and InAs/In(x)Ga(1-x)Sb Superlattice IR Detectors," *Electrochemical Society Proceedings*, vol. 95-28, pp. 211–218, 1995.

[52] C. M. Ciesla, B. N. Murdin, C. R. Pidgeon, R. a. Stradling, C. C. Phillips, M. Livingstone, I. Galbraith, D. A. Jaroszynski, C. J. G. M. Langerak, P. J. P. Tang, and M. J. Pullin, "Suppression of Auger recombination in arsenic-rich $InAs_{1x}Sb_x$ strained layer superlattices," *Journal of Applied Physics*, vol. 80, no. 5, 1996.

[53] Y. Aytac, B. V. Olson, J. K. Kim, E. A. Shaner, S. D. Hawkins, J. F. Klem, M. E. Flatté, and T. F. Boggess, "Temperature-dependent optical measurements of the dominant recombination mechanisms in InAs/InAsSb type-2 superlattices," *Journal of Applied Physics*, vol. 118, no. 12, 2015.

[54] E. H. Steenbergen, Z. Lin, S. Elhamri, W. C. Mitchel, Y.-H. Zhang, and R. Kaspi, "Effects of AlSb interfaces on InAs/InAsSb type-II infrared superlattice material properties," *Proceedings of SPIE: Infrared Technology and Applications XLI*, vol. 9451, 2015.

[55] O. O. Cellek, H. Li, X.-M. Shen, Z. Lin, E. H. Steenbergen, D. Ding, S. Liu, Q. Zhang, H. S. Kim, J. Fan, M. J. DiNezza, W. H. G. Dettlaff, P. T. Webster, Z. He, J.-J. Li, S. R. Johnson, D. J. Smith, and Y.-H. Zhang, "InAs/InAsSb Type-II superlattice: a promising material for mid-wavelength and long-wavelength infrared applications," *Proceedings of SPIE: Infrared Technology and Applications XXXVIII*, vol. 8353, 2012.

[56] H. S. Kim, O. O. Cellek, Z.-Y. Lin, Z.-Y. He, X.-H. Zhao, S. Liu, H. Li, and Y.-H. Zhang, "Long-wave infrared nBn photodetectors based on InAs/InAsSb type-II superlattices," *Applied Physics Letters*, vol. 101, 2012.

[57] T. Schuler-Sandy, S. Myers, B. Klein, N. Gautam, P. Ahirwar, Z.-B. Tian, T. Rotter, G. Balakrishnan, E. Plis, and S. Krishna, "Absorber Doping in Gallium-Free Superlattice Photodetectors." Presented at the US Workshop on the Physics & Chemistry of II-VI materials, Chicago, Il., Oct. 2013.

[58] T. Schuler-Sandy, M. Malone, Z. Tian, L. Treider, E. Plis, T. Rotter, C. Morath, V. Cowan, and S. Krishna, "Gallium free type II InAs/$InAs_xSb_{1-x}$ superlattice photodetectors," *Applied Physics Letters*, vol. 101, 2012.

[59] E. A. Plis, T. Schuler-Sandy, D. A. Ramirez, S. Myers, and S. Krishna, "Dark current reduction in InAs/InAsSb superlattice mid-wave infrared detectors through restoration etch," *Electronics Letters*, October 2015.

[60] A. Haddadi, R. Chevallier, G. Chen, A. M. Hoang, and M. Razeghi, "Bias-selectable dual-band mid-/long-wavelength infrared photodetectors based on InAs/InAs1xSbx type-II superlattices," *Applied Physics Letters*, vol. 106, 2015.

[61] Y. Huang, J. H. Ryou, R. D. Dupuis, V. R. D'costa, E. H. Steenbergen, J. Fan, Y. H. Zhang, A. Petschke, M. Mandl, and S. L. Chuang, "Epitaxial growth and characterization of InAs/GaSb and InAs/InAsSb type-II superlattices on GaSb substrates by metalorganic chemical vapor deposition for long wavelength infrared photodetectors," *Journal of Crystal Growth*, vol. 314, no. 1, pp. 92–96, 2011.

[62] Z.-D. Ning, S.-M. Liu, S. Luo, F. Ren, F. Wang, T. Yang, F.-Q. Liu, Z.-G. Wang, and L.-C. Zhao, "Growth and characterization of InAs/InAsSb superlattices by metal organic chemical vapor deposition for mid-wavelength infrared photodetectors," *Materials Letters*, 2015.

[63] kSA 400, . Dexter, MI: k-Space Associates, Inc.

[64] M. Sardela, "X-ray analysis methods." Presented at the 6^{th} Advanced Materials Characterization Workshop, Urbana-Champaign, Il., June 2012.

[65] S. Liu, H. Li, O. O. Cellek, D. Ding, X.-M. Shen, Z.-Y. Lin, E. H. Steenbergen, J. Fan, Z.-Y. He, J. Lu, S. R. Johnson, D. J. Smith, and Y.-H. Zhang, "Impact of substrate temperature on the structural and optical properties of strain-balanced InAs/InAsSb type-II superlattices grown by molecular beam epitaxy," *Applied Physics Letters*, vol. 102, 2013.

[66] H. Haugan, K. Mahalingam, F. Szmulowicz, and G. Brown, "Quantitative study of the effect of deposition temperature on antimony segregation in gallium-free InAs/InAsSb superlattices," *Journal of Crystal Growth*, 2015.

[67] H. Haugan, F. Szmulowicz, K. Mahalingam, G. J. Brown, S. L. Bowers, and J. A. Peoples, "Compositional control of the mixed anion alloys in gallium-free InAs/InAsSb superlattice materials for infrared sensing," *Proceedings of SPIE: Infrared Sensors, Devices, and Applications V*, vol. 9609, 2015.

[68] R. Kaspi and G. Donati, "Digital alloy growth in mixed As/Sb heterostructures," *Journal of Crystal Growth*, vol. 251, no. 1-4, pp. 515–520, 2003.

[69] Y.-h. Zhang and D. H. Chow, "Improved crystalline quality of AlAsxSb(1-x) grown on InAs by modulated molecular-beam epitaxy," *Applied Physics Letters*, vol. 65, 1994.

[70] Y.-H. Zhang, "Accurate control of As and Sb incorporation ratio during solid-source molecular-beam epitaxy," *Journal of Crystal Growth*, vol. 150, pp. 838–843, 1995.

[71] L. Ouyang, E. H. Steenbergen, Y.-H. Zhang, K. Nunna, D. L. Huffaker, and D. J. Smith, "Structural properties of InAs/$InAs_{1-x}Sb_x$ type-II superlattices grown by molecular beam epitaxy," *Journal of Vacuum Science and Technology B*, vol. 18, no. 2, pp. 746–750, 2000.

[72] H. Li, S. Liu, O. O. Cellek, D. Ding, X.-M. Shen, E. H. Steenbergen, J. Fan, Z. Lin, Z.-Y. He, Q. Zhang, P. T. Webster, S. R. Johnson, L. Ouyang, D. J. Smith, and Y.-H. Zhang, "A calibration method for group V fluxes and impact of V/III flux ratio on the growth of InAs/InAsSb type-II superlattices by molecular beam epitaxy," *Journal of Crystal Growth*, vol. 378, 2013.

[73] G. Dente and M. Tilton, "Pseudopotential methods for superlattices: Applications to mid-infrared semiconductor lasers," *Journal of Applied Physics*, vol. 86, no. 3, 1999.

[74] G. Dente and M. Tilton, "Comparing pseudopotential predictions for InAs/GaSb superlattices," *Physical Review B*, vol. 66, no. 16, 2002.

[75] O. Klin, N. Snapi, Y. Cohen, and E. Weiss, "A study of MBE growth-related defects in InAs / GaSb type-II supperlattices for long wavelength infrared detectors," *Journal of Crystal Growth*, vol. 425, pp. 54–59, 2015.

[76] P. Barman and S. Basu, "Thermal oxidation of gallium antimonide - surface studies of the substrate and oxide film," *Applied Surface Science*, vol. 55, 1992.

[77] D. C. Look, "Defects in Low-Temperature-Grown MBE GaAs," in *MRS Proceedings* (H. J. von Bardeleben, M. Lannoo, M. O. Manasreh, and G. S. Pomrenke, eds.), vol. 325, 1993.

[78] H. Malm, R. M. von Würtemberg, C. Asplund, H. Martijn, A. Karim, O. Gustafsson, E. Plis, and S. Krishna, "Recent developments in type-II superlattice detectors at IRnova AB," *Proceedings of SPIE: Infrared Technology and Applications XXXVIII*, vol. 8353, 2012.

[79] A. S. Gilmore, J. Bangs, and A. Gerrish, "Current voltage modeling of current limiting mechanisms in HgCdTe focal plane array photodetectors," *Journal of Electronic Materials*, vol. 34, no. 6, pp. 913–921, 2005.

[80] E. H. Steenbergen, S. Elhamri, T. J. Asel, W. C. Mitchel, S. T. Hierath, and G. J. Brown, "Impact of Be-doping on the material properties of InAs/InAsSb type-II superlattices for infrared detection," *Proceedings of the SPIE*, vol. 8993, 2014.

[81] D. Hoffman, B. M. Nguyen, P. Y. Delaunay, A. Hood, M. Razeghi, and J. Pellegrino, "Beryllium compensation doping of InAsGaSb infrared superlattice photodiodes," *Applied Physics Letters*, vol. 91, 2007.

[82] E. H. Steenbergen, S. Elhamri, W. C. Mitchel, S. Mou, and G. J. Brown, "Carrier transport properties of Be-doped InAs/InAsSb type-II infrared superlattices," *Applied Physics Letters*, vol. 104, 2014.

[83] T. Schuler-Sandy, B. Klein, L. Casias, S. Mathews, C. Kadlec, Z. Tian, E. Plis, S. Myers, and S. Krishna, "Growth of InAs-InAsSb SLS through the use of digital alloys," *Journal of Crystal Growth*, vol. 425, pp. 29–32, 2015.

[84] K. Mahalingam, E. H. Steenbergen, G. J. Brown, and Y.-h. Zhang, "Quantitative analysis of strain distribution in $InAs/InAs_{1-x}Sbx$ superlattices," *Applied Physics Letters*, vol. 103, 2013.